Catalysis Science & Technology

Accepted Manuscript

ROYAL SOCIETY OF CHEMISTRY

www.rsc.org/catalysis

Catalysis Science & Technology

RSCPublishing

PERSPECTIVE

Developments and perspectives of oxide-based catalysts for the oxygen evolution reaction

Cite this: DOI: 10.1039/xoxxooooox

E. Fabbri, A. Habereder, K. Waltar, R. Kötz, and T. J. Schmidt

Received ooth January 2012,
Accepted ooth January 2012

DOI: 10.1039/xoxxooooox

www.rsc.org/

The growing need to store large amount of energy produced from renewable sources has recently directed substantial R&D efforts toward water electrolysis technologies. Although the description of the electrochemical reaction of water electrolysis dates back to the late XVIII century, improvements in terms of efficiency and stability are foreseen for a widespread market penetration of water electrolysers. Particular advances are required for the electrode materials catalysing the oxygen evolution reaction (OER) at the anode side which has slow kinetics and, thus, is one of the major sources of the cell efficiency loss. In the recent years, high-level theoretical tools and computational studies have led to significant progresses in the atomic level understanding of the OER and electrocatalyst behaviour. In parallel, several experimental studies have explored new catalytic materials with advanced properties and kinetics on a technical-relevant level. This contribution summarises previous and the most recent theoretical predictions and experimental outcomes in the field of oxide-based catalysts for the OER, both operating in acidic and alkaline environment.

1 Introduction

To support a sustainable economic growth, it becomes more and more important that the energy utilization efficiency and the renewable energy implementation should be further exploited. Primary renewable energy sources, such as wind and solar power, have the advantages of being sustainable and relatively benign in term of impact on the environment and the human health. However, a significant disadvantage of most renewable energy sources is that they are intermittent on daily, seasonal and also regional scale with considerable variability in supply. This uncertainty in energy supply can be eliminated by connecting a local energy storage system to the electricity production unit.[1] In this framework, water electrolysers can play a fundamental role in the development of a sustainable energy system. Water electrolysers are electrochemical energy conversion devices producing hydrogen (and oxygen) from the intermittent energy source. The hydrogen energy vector represents an alternative to electricity storage in batteries, since its reconversion into electricity via fuel cells opens up independent scaling of power and energy due to the separation of the hydrogen storage from the conversion device.

Since its first observation by van Trostwijk and Deiman in 1789 [2, 3] water electrolysis has been investigated in depth, but still substantial efforts are needed to meet the requirements for practical applications. In fact, while possessing the advantages of flexibility, almost zero-emissions, and production of high purity gases, water electrolysis needs to be improved in terms of efficiency and durability to become economically attractive.[1]

The main classification of water electrolysers can be done on the basis of the operating temperature and electrolyte nature. Low temperature electrolysers can be subdivided in (acidic) polymer electrolyte water electrolysers (PEWEs) and alkaline water electrolysers (AWEs). PEWEs use a solid polymer electrolyte which selectively conducts positive ions such as protons and creates a local acidic environment. The main advantages of PEWEs are fast kinetics of the cathodic hydrogen evolution reaction and high voltage efficiencies at high current densities. Furthermore, they can produce pure hydrogen at relative high pressures with over 150 bar being demonstrated,[4] offering the possibilities of storing hydrogen directly without or only with small further mechanical compression.[4, 5] However, under the typical operation conditions of a PEWE only few electrode materials can present adequate stability. Therefore the anodic and cathodic reaction is generally catalysed by noble metal-based catalysts such as Pt, Ru and Ir. The main advantage of AWEs is the possibility of using alternative catalysts to noble metals and cheap flow fields since several materials present adequate stability in contact with an alkaline electrolyte. Furthermore, the alkaline medium allows a more favourable oxy-

gen electrocatalysis at the anode side compared to the acidic one.[6]

Overall, the cathodic and anodic reactions occurring at the PEWE and AWE electrodes can be described by the following equations:

PEWEs $4e^- + 4H^+ \rightarrow 2H_2 \uparrow$ cathode
$2H_2O \rightarrow 4H^+ + 4e^- + O_2 \uparrow$ anode

AWEs $4e^- + 4H_2O \rightarrow 4OH^- + 2H_2 \uparrow$ cathode
$4OH^- \rightarrow 2H_2O + 4e^- + O_2 \uparrow$ anode

Common to both PEWEs and AWEs is the significant overpotential occurring at the anode side where the oxygen evolution reaction (OER) takes place. For that reason, the OER has been intensively studied for many decades in order to elucidate the reaction mechanism and to minimise the energy loss during water electrolysis. Improving OER kinetics would indeed favour a widespread market penetration of both PEWEs and AWEs. The catalyst that generally shows the best trade-off between catalytic activity and stability, both in acidic and alkaline media, is IrO_2. However, since iridium is quite expensive and, as a typical secondary metal, resource limited,[7] many research efforts have been directed towards the development of OER catalysts with reduced amount of Ir or based on other transition metal oxides. This is particularly the case for AWEs since base metals, such as cobalt, nickel and perovskite oxides, proved to be quite stable and active in alkaline media.

In the present perspective, current issues and recent developments in catalyst materials for the OER will be summarised and discussed. Particularly fundamental aspects of the OER will be addressed as well as practical requirements for oxygen evolution catalysts. Selected catalyst materials, both for PEWE and AWE applications, will be also described in details. All catalyst materials will be examined as *oxides* since the high anodic potentials during water electrolysis inevitably lead to oxidation of the electrode material even when studies are started with pure metals.

2 Mechanistic insight into oxygen evolution reaction

2.1 Definition of catalytic activity and kinetic parameters for the OER

A good survey on oxygen evolution catalysis was published in 1986 by Matsumoto and Sato.[8] In this review and in many other studies, the Tafel slope has often been used to compare the catalytic activity towards the OER of catalysts. For multistep reaction mechanisms the Tafel slope is defined as the dependency of the ohmic drop corrected overpotential η on the current density j:

$$\frac{d\lg(j)}{d\eta} = \frac{2.3 \times RT}{\alpha z F} \quad (1)$$

Whereupon R is the ideal gas constant and F is the Faraday constant. At constant temperature T, the slope is only dependent on the reaction mechanism, which corresponds to the product of the transfer coefficient α and the number of transferred electrons z in the rate determining step (RDS). Besides containing important information about the reaction mechanism, the value of the Tafel slope represents an important parameter, particularly from application point of views, to estimate the performance of an OER catalyst; indeed, the Tafel slope indicates the current density changes with increasing overpotential. However, considering only the value of the Tafel slope as an activity parameter for the OER does not allow overall assessment of catalyst activity. For example, if we consider the case of three catalysts showing similar Tafel slopes but different exchange current densities (j_0), the measured current densities at a defined overpotential would be quite different as shown for example in **Figure 1** for cobalt black,[9] RuO_2[10] and an iron/nickel[11] catalysts. The above example makes clear that besides the Tafel slope it is necessary to indicate an additional kinetic parameter as activity metric.

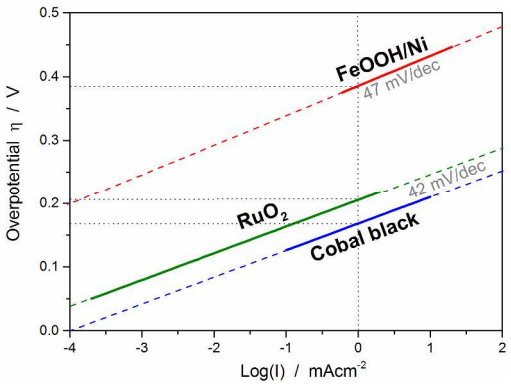

Figure 1 Sketched Tafel plots for three different catalysts based on activity data from literature: Cobalt black (40wt% KOH at 80 °C),[9] RuO_2 (1 M H_2SO_4 at 20 °C)[10] and a composite electrode consisting of FeOOH nanowires and Ni foam (0.1 M NaOH)[11]. Even if the values of the Tafel slope for the three catalysts are quite similar, the exchange current density or the overpotential at a certain current density (here selected as at 1 mA/cm^2) can show significant differences.

In case of the oxygen reduction reaction (ORR), in order to compare the activity of different catalysts it is widely common and accepted to consider the kinetic current at 0.9 V (RHE) as activity parameter where the effects of mass transport limitations are almost negligible.[12] Differently, in the case of the OER, besides the Tafel slope, there is not a *common* parameter to describe the activity of different catalysts. Different kinetic parameters can be used in combination with or without the Tafel slope to define the activity of oxygen evolution catalysts. In the following we examine different options, evaluating advantages and disadvantages of different activity parameters. **Table 1** gives an overview of possible parameters that could be used in combination with the Tafel slope to characterise the catalytic activity of a catalyst material towards the OER.

For highly irreversible reaction like the OER or the ORR, the exchange current density j_o cannot be used as the intrinsic factor of catalyst activity since its experimental determination is

Table 1 Possible kinetic parameters to use in combination with the Tafel slope to describe the catalytic activity towards the OER of different catalyst materials.

Parameter	Symbol
Exchange current density	j_0
Potential at a defined current density	$\phi(j)$ e.g. *at* $10\ A/g_{metal}$
Current density at a defined potential	$j(\phi)$

highly erroneous. The value of j_o can be obtained by extrapolating the Tafel plot at zero overpotential. Due to the logarithmic scale of the current axis very small inaccuracies in the Tafel slope, i.e. deriving from the ohmic drop correction or the linear fitting, can lead to large errors in the exchange current density estimation. In addition, due to the high irreversibility of the reaction, extrapolations towards the equilibrium potential have to be performed over many orders of magnitude in current density, increasing the error bars for the j_o values. For the alternative parameters the main disadvantage is that their values are strongly dependent on the measuring conditions, such as the scan rate or the direction of the potential sweep (anodic or cathodic direction). To eliminate this issue, an accurate way is to measure current or potential response potentiostatically or galvanostatically, respectively. After a short holding time almost steady-state conditions can be achieved[13] and the appearing signal is mainly controlled by the kinetics of the OER. Therefore, the measurements of the steady-state current at defined potential or the potential at defined steady-state current together with the value of the Tafel slope might represent a valid couple of activity parameters. Although rather arbitrary, among different possible combinations, we would like to propose as activity parameters the Tafel slope combined with the potential value measured at 10 A/g_{metal}. Particularly, we have selected as activity parameter the potential at a certain current value normalised by the catalyst (metal) mass and not by the geometric area, roughness factor, or catalyst surface area for reasons that will be explained in the following:

(i) The potential at steady-state current density with geometric surface area normalisation cannot be used as an activity parameter because it does not take into account the catalyst loading. For example, samples of the same material can show different potentials at a defined mA/cm^2_{geo} depending on the amount of catalyst used.

(ii) The current normalization by the catalyst roughness factor or electrochemical active surface area (i.e., the specific current density) can provide the intrinsic value of the materials catalytic activity. However, for most of the investigated catalysts it is rather non-trivial to determine the roughness factor with reasonable accuracy either by cyclic voltammetry or impedance spectroscopy, and even an optimised procedure leads to accuracies within an order of magnitude.[14] Therefore, despite the current normalisation by the catalyst roughness factor would represent the best choice as activity parameter, analogous to the case of the ORR, at the moment this parameter is not (yet) experimentally accurate.

(iii) The potential measured at a current normalised by the surface area of the catalyst, i.e. measured by Brunauer–Emmett–Teller (BET) analysis, could be also a good activity parameter for many catalyst materials. However, not always the BET surface area corresponds to the electrochemical active surface area of the catalyst. For example, in case of ABO_3 perovskite catalysts, the active site is mostly considered to be the B-site cation of the perovskite structure.[15, 16] Therefore, considering the current normalised by the BET surface area would not allow a fair comparison between catalysts with different surface densities of active sites.

(iv) The turnover frequency (TOF) would be a good candidate as an activity parameter since it also provides the intrinsic catalytic activity; however, as for the calculation of the roughness factor, the evaluation of the electrochemical active sites is still rather an issue.

We are aware that there are also drawbacks related to the use of the potential at fixed mass normalised current (mass specific current density) as activity parameter. It does not represent the intrinsic catalytic activity of the material and it does not allow a fair comparison of the catalytic activity between catalysts with significantly different particle size and/or molecular mass. Furthermore, it does not allow a direct comparison with the theoretical activities, which are generally normalized by active sites. However, in the view of the previous discussion we believe that at present it represents the activity parameter least affected by experimental inaccuracies, together with the Tafel slope. For the measurement of the Tafel slope we recommend a low scan rate (below 5 mV/s) or even better a quasi-stationary current/potential curve, i.e. holding the potential until an almost steady state current is achieved (the holding time mostly depends on the material properties). **Figure 2** shows a comparison between the Tafel curves of a commercial $IrTiO_2$ electrode (Umicore AG & Co) obtained by a cyclic voltammetry measurement at 5mV/s and by a chronoamperometry experiment holding each potential for 30 sec in 20% O_2-saturated 0.1 M $HClO_4$. As shown in Figure 2, a chronoamperometry measurement eliminates capacitive current effects (see potential region between 1.4-1.5 vs. RHE in **Figure 2**), allowing a more reliable analysis of the Tafel slope.

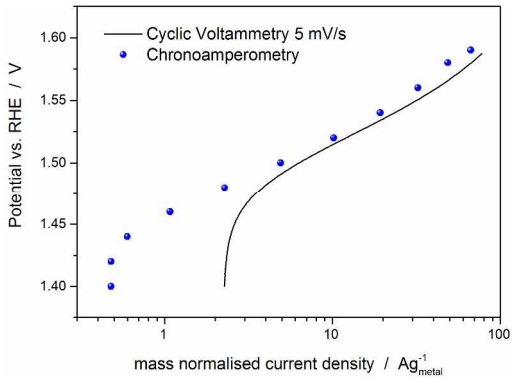

Figure 2 Tafel curves of commercial $IrTiO_2$ electrode (Umicore AG & Co) obtained by a cyclic voltammetry measurement at 5mV/s and by a chronoamperometry experiment holding each potential for 30 sec in 20% O_2-saturated 0.1 M $HClO_4$ at room temperature and rotation speed of 900 rpm.

2.2 Reaction mechanism and main parameters influencing the OER kinetics and thermodynamics

In the 1986 Matsumoto and Sato[8] summarised the different reaction mechanisms proposed for the OER in acidic as well as in alkaline media (**Table 2**). In the described mechanistic pathways the "S" characterises the catalytically active site. In acid solution, the most recognised mechanisms are the electrochemical oxide path and the oxide path. In alkaline solutions, all the proposed reaction mechanisms have the initial adsorption of the hydroxide ions on the catalytically active site as a common step, followed by different intermediate reaction steps. Overall, both in acidic and in alkaline environment the proposed mechanistic schemes for the OER comprise different elementary reaction steps and involve several surface adsorbed intermediates. The overall reaction overpotential is commonly thought to be related to the kinetic constraints of the individual reaction steps.[17] The elementary reaction step with the highest kinetic activation barrier is generally defined as the rate determining step (RDS). While for many years the RDS has been a central topic, recently the attention has been additionally pointed towards the potential determining step (PDS) which highlights more the thermochemical aspects of the OER overpotential.[17-23] The PDS represents the step with the maximum change of Gibbs free chemisorption energy of two subsequent adsorbed intermediates (ΔG^{max}). The theoretical overpotential (η^{OER}) related to the PDS can be calculated at standard conditions and U = 0 V vs. SHE as:[18]

$$\eta^{OER} = \left(\frac{\Delta G_{max}}{e}\right) - 1.23\ V \qquad (2)$$

For an ideal catalyst the ΔG associated to each elementary reaction step is equal to 1.23 eV as estimated by Man et al.[18] by DFT calculations at pH = 0, standard conditions, and cell potential of U = 0 V vs. SHE (**Figure 3a**). In this ideal case there will be no overpotential due to thermodynamic hindrance. Clearly, this scenario does not consider kinetic barriers. Furthermore, the DFT calculations are based on the assumption that the OER follows a four step mechanism described by the equations (3)-(6) described in **Table 3**[18] where $\Delta G_{1\text{-}4}$ denotes the standard Gibbs Energy change of the reaction and $\Delta G_{oxygenated\ species}$ denotes the standard Gibbs Energy of formation of the respective species.

Table 2 Possible reaction mechanisms of the oxygen evolution reaction on oxides as reported by Matsumoto and Sato.[8]

Acid solution

A Electrochemical oxide path[24]
- (a) $^{a}S + H_2O \rightarrow S\text{-}OH + H^+ + e^-$
- (b) $S\text{-}OH \rightarrow S\text{-}O + H^+ + e^-$
- (c) $2S\text{-}O \rightarrow 2S + O_2$

B Oxide path[24]
- (a) $S + H_2O \rightarrow S\text{-}OH + H^+ + e^-$
- (b) $2S\text{-}OH \rightarrow S\text{-}O + S + H_2O$
- (c) $2S\text{-}O \rightarrow 2S + O_2$

C Krasil'shchkov path[25]
- (a) $S + H_2O \rightarrow S\text{-}OH + H^+ + e^-$
- (b) $S\text{-}OH \rightarrow S\text{-}O^- + H^+$
- (c) $S\text{-}O^- \rightarrow S\text{-}O + e^-$
- (d) $2S\text{-}O \rightarrow 2S + O_2$

D Wade and Hackerman's path[26]
- (a) $2S + 2H_2O \rightarrow SO + SH_2O + 2H^+ + 2e^-$
- (b) $SO + 2SOH^- \rightarrow 2S + SH_2O + O_2 + 2e^-$

Alkaline solution

E Electrochemical oxide path[24]
- (a) $S + OH^- \rightarrow S\text{-}OH + e^-$
- (b) $S\text{-}OH + OH^- \rightarrow S\text{-}O + H_2O + e^-$
- (c) $2S\text{-}O \rightarrow 2S + O_2$

F Oxide path[24]
- (a) $S + OH^- \rightarrow S\text{-}OH + e^-$
- (b) $2S\text{-}OH \rightarrow S\text{-}O + S + H_2O$
- (c) $2S\text{-}O \rightarrow 2S + O_2$

G Krasil'shchkov path[25]
- (a) $S + OH^- \rightarrow S\text{-}OH + e^-$
- (b) $S\text{-}OH + OH^- \rightarrow S\text{-}O^- + H_2O$
- (c) $S\text{-}O^- \rightarrow S\text{-}O + e^-$
- (d) $2S\text{-}O \rightarrow 2S + O_2$

H Yeager's path[27, 28]
- (a) $S + OH^- \rightarrow S\text{-}OH + e^-$
- (b) $S^z\text{-}OH \rightarrow S^{z+1}\text{-}OH + e^-$
- (c) $2S^{z+1}\text{-}OH + 2OH^- \rightarrow 2S + 2H_2O + O_2$

I Bockris path[15]
- (a) $S + OH^- \rightarrow SOH + e^-$
- (b) $SOH + OH^- \rightarrow S\text{-}H_2O_2 + e^-$
- (c) $S\text{-}H_2O_2 + OH^- \rightarrow S\text{-}O_2H^- + H_2O$
- (d) $S\text{-}H_2O_2 + S\text{-}O_2H^- \rightarrow H_2O + OH^- + O_2$

^{a}S represents a surface active site

Table 3 A four step reaction mechanism for the OER proposed by Man et al.[18]. $\Delta G_{1\text{-}4}$ denotes the standard Gibbs Energy change of the reaction, whereas $\Delta G_{\text{oxygenated species}}$ denotes the standard Gibbs Energy of formation of the respective species. The results of the DFT calculations shown in **Figure 3** are based on the assumption that the OER follows the paths described by Equations (3)-(6).

$H_2O\ (l) + S \rightleftharpoons HO^* + H^+ + e^-$ $\Delta G_1 = \Delta G_{HO^*} - \Delta G_{H_2O\ (l)} - eU + k_b T\ ln a_{H^+}$	(3)
$HO^* \rightleftharpoons O^* + H^+ + e^-$ $\Delta G_2 = \Delta G_{O^*} - \Delta G_{HO^*} - eU + k_b T\ ln a_{H^+}$	(4)
$O^* + H_2O\ (l) \rightleftharpoons HOO^* + H^+ + e^-$ $\Delta G_3 = \Delta G_{HOO^*} - \Delta G_{O^*} - eU + k_b T\ ln a_{H^+}$	(5)
$HOO^* \rightleftharpoons S + O_2(g) + H^+ + e^-$ $\Delta G_4 = \Delta G_{O_2} - \Delta G_{HOO^*} - eU + k_b T\ ln a_{H^+}$	(6)

Differently from the case of an ideal catalyst where the ΔG associated to each elementary reaction step is equal to 1.23 eV, a real catalyst generally presents a PDS with a larger ΔG. **Figure 3b** shows as an example the case of $LaMnO_3$ catalysts;[18] the ΔG between the reaction steps associated to O* and HOO* reaction intermediates (reaction (5) in **Table 3**) is the largest and thus it represents the thermochemical less favourable step (PDS).[18] Improved catalytic activity towards the OER using the aforementioned catalyst could be achieved by reducing the ΔG associated to the peroxide formation. However, for several types of catalysts (rutile, perovskite, spinel, rock salt, and bixbyite) a linear scaling relation exists between the chemisorption energies of the different surface intermediates,[18] i.e. if the energy associated to one reaction step is changed, the others do too. It was pointed out by Koper[19] and by Man et al.[18] that the binding energies of HO* and HOO* are related to each other by a constant energy value of approximately 3.2 eV at U=0 V (see **Figure 3b**), both in case of metals and oxide surfaces and regardless of the binding site. Since that difference is higher than the ideal one (2.46 eV, see **Figure 3a**), a real catalyst generally shows a minimum theoretical overpotential. Based on this predicted linear scaling relation, the best approximation to an ideal catalyst for the OER would be a material able to minimize the unfavourable energetic relationship between intermediates. The linear scaling between the intermediate bonding strengths also implies that the OER activity can be plotted as a function of the

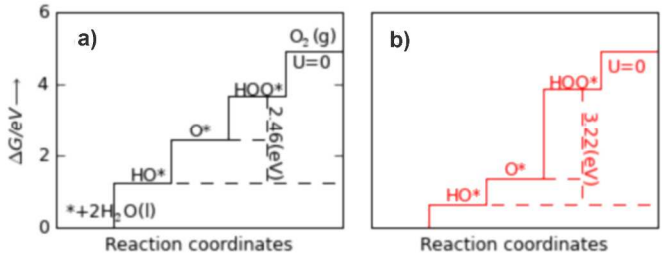

Figure 3 Standard free energies at U=0 V for an ideal catalyst (a) and for $LaMnO_3$ (b). For real catalysts, $\Delta G^0_{HOO^*} - \Delta G^0_{HO^*}$ (vertical dashed lines) is approximately constant with an average value of 3.2 eV, whereas the ideal value is 2.46 eV. Reproduced with permission of ref. [18].

adsorption energy of only one involved species, for example the O* species. **Figure 4** shows the theoretical activity of the four reaction steps described by equations (3)-(6) as function of the oxygen binding energy.[23] Materials with high catalytic activity towards the OER would stay on the horizontal dashed line (representing the equilibrium potential) and present an O* binding energy of around 2.3 eV. The volcano plot in bottom part of **Figure 4** also indicates that for weak and strong O* surface binding energy the OER activity would be limited by the O* (red line) and by the HOO* (green line) formation step, respectively.[23] For example, RuO_2 binds oxygen a little too weakly, while IrO_2 binds O* too strongly.[23] A similar concept of a single microscopic parameter governing the oxygen evolution activity was already introduced in the early 1980's by Brockis and Otagawa[15] and by Trasatti.[29] Brockis and Otagawa[15] proposed a correlation between the catalytic activity (experimentally measured Tafel slope or current density at a defined overpotential) of $LaBO_3$ perovskites and the B-OH bonding strength, as well as between the catalytic activity and the number of electrons occupying the antibonding orbitals (discussed in detail in section 4.4).[15]

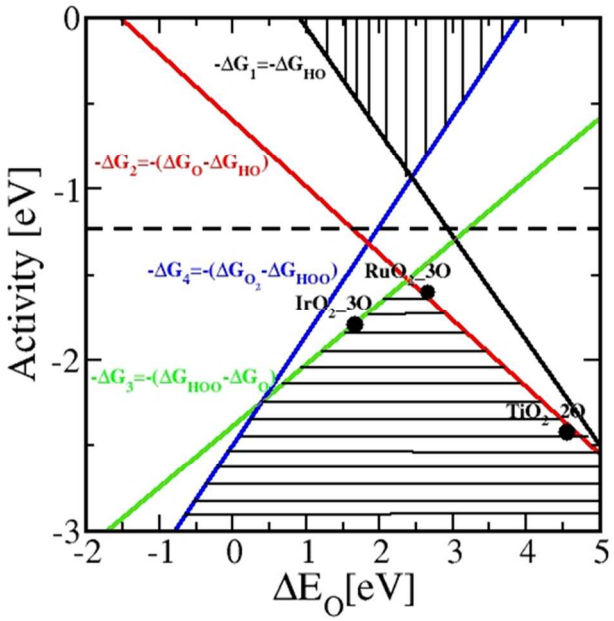

Figure 4 Theoretical OER activity, defined as the negative change of the Gibbs free energy, -ΔG, of the four reaction steps described in equations (3)-(6) as a function of the oxygen binding energy. Reproduced with permission of ref. [23].

In a more recent work of Man et al.[18] the difference between the energy states of two sequent intermediates ($\Delta G^0_{HOO^*} - \Delta G^0_{HO^*}$) has been taken as a descriptor for the catalytic activity of several different compounds revealing a volcano relationship (**Figure 5**). The difference of the bonding strength responds to the Sabatier principle:[30] In case of surfaces that bind oxygen too weakly, intermediates cannot easily react and the potential is limited by the oxidation of HO*. In the opposite case of strong oxygen bonding, the intermediate states and the adsorbed products are quite stable and the potential is limited by the formation of HOO* species. The optimum case is therefore a

mean bonding strength, such as in the case of RuO_2, Co_3O_4, NiO, PtO_2, $SrCoO_3$, $LaNiO_3$, $SrCoO_3$ and $SrNiO_3$ (top of the volcano plots in **Figure 5**).

Besides the importance of the binding energy of the reaction intermediates, the specific adsorption of ions from the electrolyte can also play a critical role in the OER. Adsorption of anionic impurities on the catalyst surface can block part of the electrocatalytic active sites and hinder the oxygen evolution reaction. While the influence of spectator adsorption on the catalytic activity towards the ORR has been investigated in detail,[31, 32] in case of the OER only little work has been carried out so far. However, also this aspect may be crucial in developing advanced catalysts with designed electrochemical interface.[17]

To this point we have discussed the importance in understanding the RDS, the bonding strength of reaction intermediates and presence of anion adsorbates for the OER. A different aspect worth to consider is the nature of the electrochemical interface created at the surface of metal oxides in contact with an aqueous electrolyte. Several oxides used as catalysts for the OER possess metallic electronic conductivity (e.g. RuO_2, IrO_2 and $LaNiO_3$) which reduces the ohmic drop in the electrode bulk material. Besides these materials, also n- and p-type semiconducting oxides (e.g. NiO, Co_3O_4 and $LaCoO_3$) have been widely investigated as oxygen evolution catalysts. When a metal or a semiconductor electrode is inserted in an electrolyte an electrical double layer is formed. Compared to metals, semiconductors provide much lower charge carrier concentration and thus a large space charge layer is formed at the surface. In general, at anodic potentials typical for the OER the potential drop in the space charge layer will be negligible for the p-type semiconductor due to the accumulation of holes at the surface. Contrarily, in the case of n-type semiconductors the space charge layer at the interface leads to an additional barrier for charge carriers.[8] Therefore p-type semiconducting oxides or metallic-like oxide conductors should be more suitable catalyst materials for the OER than n-type semiconductors.[8]

2.3 Requirements for oxygen evolution catalysts

Besides a high catalytic activity, an optimal catalyst material must fulfil also other requirements. High surface area is generally required since it allows minimising the amount of required catalyst, particularly when noble metal-based catalysts are used.[29] A common way to achieve a high surface area is to use porous powders synthesized by wet chemistry methods. It is worth to highlight that the *specific surface area* must not be confused with the *active area*, i.e. the number of active sites involved in the electrocatalytic reaction. Therefore, a high specific surface area might not be directly turned into a high surface density of active sites. Beyond the specific surface area, also a high electrical conductivity at high electrode potentials (where oxidation state can change compared to the equilibrium state) is required to minimise the ohmic drop in the material.[29]

Another central aspect in the development of advanced catalyst materials for the OER is the catalyst current selectivity. Indeed, anodic currents at high potentials (i.e. above 1.4 V vs. RHE) can either result from the occurrence of the OER or from catalyst and/or support oxidation/corrosion. Furthermore, analogous to the case of the ORR, a certain catalyst might oxidise water via 2 electrons instead of 4 leading to peroxide species production instead of oxygen. To differentiate the measured anodic currents, i.e. to study the catalyst current selectivity, different techniques can be used. By in-situ mass spectroscopy one can correlate the concentration of evolved oxygen to the measured current to determine the catalyst selectivity.[33] Another method to estimate the catalyst selectivity is the rotating ring disk electrode (RRDE) technique. Oxygen evolved by the catalyst can in principle be reduced on the surrounding Pt ring electrode when the latter is potentiostatically held in a potential range where oxygen reduction is purely under diffusion control.

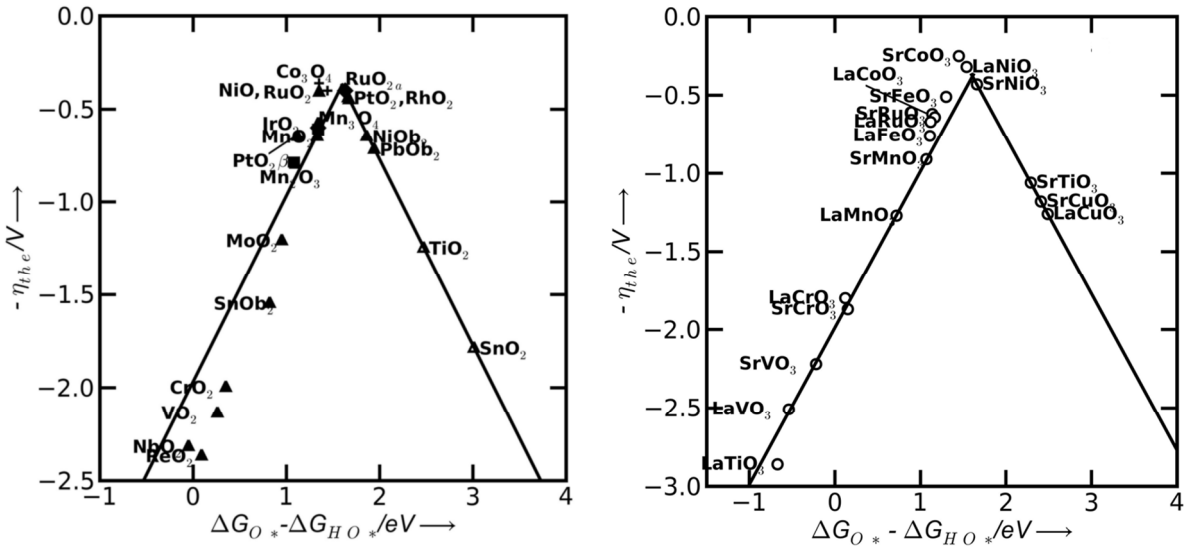

Figure 5 Theoretical overpotential for the oxygen evolution vs. the difference between the standard free energy of two sequent intermediates (ΔG°_{O*}-ΔG°_{HO}) for various binary oxides (left side) and perovskite oxide (right side). Reproduced with permission of ref. [18].

The overall number of transferred electrons $n(e^-)$ during the OER can be calculated if the disk current I_d, the ring current I_r and the setups collection efficiency N are known.[34]

$$n(e^-) = 4I_d \times N/I_r \quad (7)$$

The main issue in using RRDE for the evaluation of the catalyst selectivity is related to relatively fast local oxygen saturation and bubble formation. It has been recently suggested by McCrory et al.[14] that the optimal current density for minimising the local oxygen saturation and bubble formation at the disk electrode is 1 mA/cm_{geo}^2 at a rotation speed of 1600 rpm and in N_2 saturated electrolyte.

Another issue in water electrolysis is the wettability of the electrodes. Due to formation of molecular hydrogen and oxygen, gas bubbles form on both electrodes during water electrolysis. Unfortunately as long as they are not grown big enough, they will not detach from the surface leading to a high ohmic resistivity. At the surface which is covered by gas bubbles, the electron transfer is temporary blocked so that this catalyst surface area cannot participate in the electrocatalytic process. This also implies that high local current density can flow through part of the electrode area affecting the catalyst stability. The detachment of gas bubbles can be accelerated mechanically by circulated electrolyte. Another way is to reduce the surface tension between electrolyte and electrode. That can be either done by using additives in the electrolyte or by increasing the wettability of the catalyst material. By increasing the hydrophilicity of the catalyst material, the electrolyte can replace small gas bubbles at the catalyst surface more easily.[35] A complementary approach is to develop a material nanostructure with optimized pore size and surface area able to minimise the gas bubble growth and promote the detachment of small bubbles. For example, it has been recently shown that allowing a facile removal of gas-bubbles from the RuO_2 electrode surface improvements in catalyst activity and stability could be simultaneously achieved.[36]

Two additional requirements for a future usage in electrolysers are on one hand the health safety of the used materials. On the other hand, it is important that the raw materials for the catalyst are available and inexpensive enough for an economical large-scale production.[29]

Last but not least corrosion stability is a fundamental requirement for the implementation of a catalyst material into an operative system. During operation the anode side experiences severe oxidative conditions. Additionally, in PEWE applications the anode is also exposed to an acidic environment. Materials such as carbides or nitrides might not be used as catalysts materials because they will be generally driven to an irreversible oxidation during the OER. Also the use of carbon as catalyst support must be avoided in electrolyser applications since the high operative potential will lead to carbon oxidation and consequent failure of the anodic structure. Oxide-based catalysts can also undergo corrosion/dissolution during operation. This is for example the case of the most active oxygen evolution catalyst, RuO_2; for this catalyst material the onset of the oxygen evolution coincides with the onset of Ru corrosion.[37, 38] The detailed mechanism of oxygen evolution on RuO_2 and its stability issue will be discussed in the following section (3.1). It is worth mentioning that even though corrosion stability should be a central topic in the electrode development, only limited studies have deeply investigated the corrosion stability of oxygen evolution catalysts, both for PEWE and AWE applications. From a mechanistic point of view, also a deeper analysis to establish whether a correlation exists between the catalyst activity and the catalyst corrosion mechanism could lead to the understanding of design principles for novel catalysts and/or to the definition of the best trade-off between activity and stability.

3 Catalyst materials for polymer electrolyte water electrolysers (PEWEs)

The electrochemical splitting of water performed in acidic polymer electrolyte water electrolysers (PEWEs) has several distinct advantages as compared to alkaline systems. Superior kinetics of the cathodic hydrogen evolution reaction, high electrolyte conductivity and the potential capability to be operated at pressures above 50 bar favour its use.[4] While the cathodic hydrogen evolution takes place with excellent kinetics on Pt-based catalysts, the major challenge is to find an anodic OER catalyst offering fast kinetics and being stable in a harsh oxidising environment of low pH values and high electrode potentials. Mixed oxides of Iridium and Ruthenium are the state-of-the-art anode catalyst material in conventional PEWE technologies.[5, 39] To be applicable on a large-scale production, the amount of the noble metals Ir and Ru has to be reduced by around one order of magnitude[5] or even be avoided. Both Iridium and Ruthenium are one of the scarcest, non-radioactive metals in the earth crust and are typically produced as a side product during Pt or Ni mining. Being secondary metals, the amount of annual Ru or Ir production is only dependent on the Pt production rate, which means in turn that increasing demands of Ir or Ru will not increase their production rate, but their cost due to its coupling and dependence on the Pt or Ni mining.[7]

Therefore, in order reduce (noble metal) investment cost high efficiencies at current densities of several A/cm^2 are desirable. Tackling these issues, a main focus must be placed on the catalyst material side where the choice of composition and morphology has direct impact on the performance and costs of PEWE systems. Investigations on suitable catalyst materials for the OER in acidic electrolytes have been performed and will be reviewed in the following section with a focus on catalytic activity and stability. The catalysts are listed with respect to the number of different metallic components of which they are composed. The early investigations in this field mostly focused on metal catalysts; however, it must be considered that during potential cycling between 0.2 V and 1.4 V (RHE) most of the metal electrodes form a hydrous oxide layer at the surface,[40]

which can extend into the bulk to different degrees depending on the catalyst structure.[41] Therefore, metal catalysts are subsequently listed among the metal-oxide electrocatalysts.

3.1 Single metal(-oxide) electrocatalysts

The catalytic activities of several platinum group metal and metal-alloy catalysts in acidic solution were potentiostatically determined by Damjanovic et al.[42] The catalytic activity decreases in the order Ir > Rh > Pt, a trend which is almost opposite to the one determined for the ORR. Furthermore, an adverse effect on the OER activity has been elucidated if platinum is alloyed with catalytic superior materials.[43] Miles and Thomason[44] qualitatively confirmed Damjanovic's order of activity under galvanostatic conditions and investigated additionally ruthenium, gold and niobium. The results of their survey can be summarised in the activity order Ru > Ir > Pd > Rh > Pt > Au > Nb. These findings mostly fit the volcano plot[18] shown in **Figure 5** which indicates RuO_2 as the most active material, followed by RhO_2, IrO_2 and PtO_2.[18] Discrepancies between experimental and theoretical activity values might result from the fact that computational calculations only consider ideal surfaces and, in turn, use as activity descriptor the oxygen adsorption energy on model surfaces. However, under experimental conditions several other surface parameters (i.e. defects, crystal edges or formation of hydroxide-layers) can play a crucial role. For the same reason, depending on the processing conditions, catalyst materials with identical compositions can experimentally show different OER activities. Therefore, both theoretical and experimental results for OER catalysts should be analysed with due care since the former only considers ideal surfaces and the latter provides results strongly influenced by the catalyst preparation process and surface state.

The superior catalytic properties of Ru- and Ir-based oxides[44] in acidic environment and their high electrical conductivities[45] have shifted for decades both materials in the focus of detailed investigations as suitable oxygen evolution catalysts.

RuO_2 is generally recognised as the material showing the highest catalytic activity among the single transition metal-oxides.[29, 43, 46] Nevertheless, different activities have been reported for RuO_2 depending on processing conditions and physical-chemical properties. Single crystal samples exhibit a dissimilar Tafel behaviour depending on the crystal orientations[47] proving that similar as the ORR,[48] also the OER is a structure sensitive reaction. However, RuO_2 single crystals show worst performance for the OER than thermally prepared RuO_2 films in terms of lower onset potential and Tafel slope.[49, 50] These results indicate that the activity of polycrystalline RuO_2 cannot be solely explained by the averaged contribution of the individual crystalline orientations.[51]

The reaction mechanism of oxygen evolution on various types of RuO_2 electrodes has been experimentally investigated by several authors.[37, 52, 53] A detailed mechanism, which follows the electrochemical oxidation path described in **Table 2** has been proposed by Kötz and coworkers[37, 54] for anodically grown hydrous ruthenium oxide films and is illustrated in **Figure 6**.

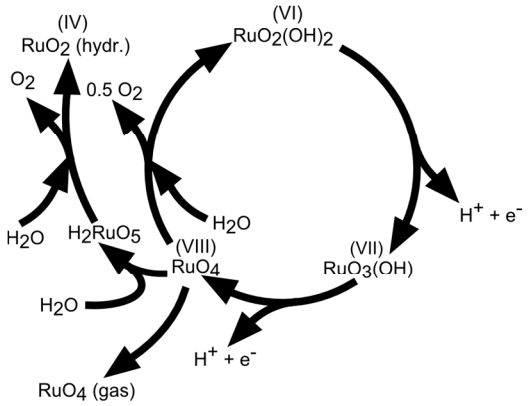

Figure 6 Sketch of the charge storage and oxygen evolution reactions on anodically grown hydrous ruthenium oxide films. Reproduced by permission of The Electrochemical Society.[37]

During potential cycling of a Ru metal electrode, the formation of a hydrous oxide layer has been detected at the surface and explained by an oxidation-reduction cycle of Ru cations. Prior to oxygen evolution, Ru is assumed to be in a VI+ oxidation state which was experimentally confirmed on thermally deposited RuO_2 films. Upon an anodic potential sweep into the oxygen evolution regime, Ru is further oxidised into an VIII+ valence state accompanied by two single deprotonating steps to keep the total charge balanced. RuO_4 then either dissociates into oxygen and the initial hydrous Ru(VI)-oxide to complete the evolution cycle or dissolves which is concomitant with a colouring of the electrolyte.[55] The existence of the ruthenate ion (VIII+) as corrosion product was verified by in-situ reflection spectroscopy and RRDE measurements.[38] It was also found that the onset of oxygen evolution coincides with the onset of Ru corrosion. It is suggested that the dissolved RuO_4 is partially redeposited on the surface. The build-up of higher valence state Ru sites at the metal-electrolyte interface during the anodic potential sweep is in agreement with mechanisms proposed by other authors.[52, 56, 57] Nevertheless, different views exist on the initial valence of the Ru sites and whether the highest valence state is achieved by electrochemical oxidation[44, 45] (electrochemical oxide path, **Table 2**) or by decomposition of adjacent hydroxyl-groups[42, 56] (oxide path, **Table 2**). There is further dispute on the amount of Ru sites involved in the charging process. Burke et al.[52] claimed that the observed charging processes are only due to redox-reactions at the hydrated oxide surface, while Galizioli et al.[49, 50] measured too large amounts of anodic charges to be simply related to surface reactions. The amount of dissolved RuO_4 in the mechanism described in **Figure 6** is directly correlated to the catalyst stability. Parts of the dissolved RuO_4 which are not recovered by redeposition get lost for further oxygen evolution. The dissolution rate is expected to depend on the stability of the intermediates being created during oxygen evolution and it has been reported to differ by orders of magnitude among anodically grown and thermally deposited oxide films.[37] Indeed, as for the activity parameters, surface morphology and stability of the catalysts

are also highly depending on the material synthesis process. However, both types of RuO_2 films are not stable under prolonged high anodic potentials above 1.4 V (RHE).[46, 58]

The other widely investigated primary electrode material is iridium oxide. Although the catalytic activities for the OER are generally inferior to those of Ru-based electrodes,[44, 46] the metallic conductivity[45] and especially its stability towards high anodic potentials in acidic environment are major advantages.[58, 59] Among the Ir-based catalysts, as in the case of Ru, differences in activity and stability arise depending on the catalyst preparation.[60] It is generally accepted that high temperature oxides with higher degree of crystallinity are less active but more stable than low temperature (amorphous) oxides[61] which exhibit a higher activity but lower stability. The fundamental origin of this reverse relationship between stability and activity for these oxides is not yet understood.

Upon potential cycling of an iridium metal electrode, a hydrous oxide layer forms at the metal-electrolyte interface,[40, 62-64] which grows into the bulk with the number of applied cycles. The growth rate of this oxide film is dependent on scan speed, sweep reverse potentials, temperature, catalyst crystallinity, morphology as well as type and concentration of electrolyte.[41, 62, 65, 66] Adversely, when the electrode potential is held constant at an anodic potential of 1.6 V (RHE) no film growth was detected.[62] The growth of an oxide layer on a sputtered Ir electrode was also confirmed by Kötz and coworkers.[40, 54] Their X-ray photoelectron spectroscopy (XPS) analysis on compositional surface changes revealed that hydroxide species are exchanged by oxide species during an anodic potential sweep. Based on these results the authors proposed an oxygen evolution mechanism on anodic grown oxide films as sketched in **Figure 7**.[40] This mechanism contains several consecutive deprotonating steps starting from an initially hydrous oxide with Ir in a 3+ valence state at potentials below 0.7 V (SCE, ~1 V vs. RHE). Ir is assumed to be in an unstable VI+ intermediate oxidation state (IrO_3) prior to dissociation to the tetravalent state as the starting point of the oxygen evolution cycle. The elucidated reaction path is in agreement with the electrochemical oxide path as described in **Table 2** and similar to the mechanism suggested for the oxygen evolution on RuO_2.[37] The catalytic activity of a metallic Ir electrode increases with the thickness of the hydrous oxide layer.[63] Frazer and Woods[67] found a higher current density at higher anodic charges which correlates to the number of potential cycles applied. Hackwood et al.[59] compared sputtered with anodically grown IrO_2 films and found higher activity on the sputtered films at small overpotentials, while the performance at high overpotentials was similar. Values of Tafel slopes of sputtered and thermally prepared IrO_2 have already been presented in a review by Matsumoto and Sato, ranging between 40 and 56 mV/dec.[8]

The stability of Ir-based electrodes has been investigated in several studies, showing that the IrO_2 catalysts generally exhibit higher corrosion stability than Ru-based ones.[46, 58, 65, 66, 68] However, the stability of IrO_2 electrodes is affect by the catalysts morphology. Long term potentiostatic treatment of

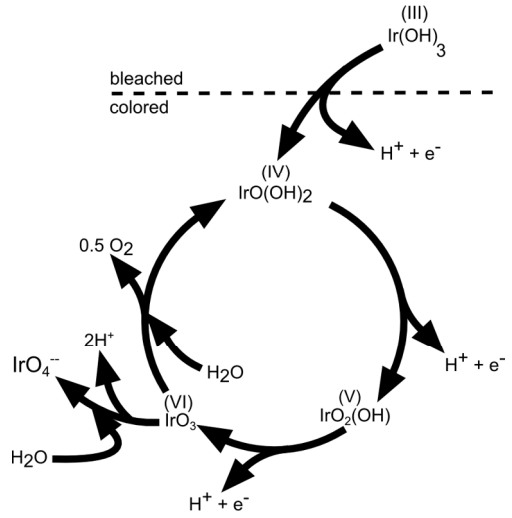

Figure 7 Sketch of the charge storage and oxygen evolution reactions on anodically grown hydrous iridium oxide films. Reproduced by permission of The Electrochemical Society.[40]

sputtered IrO_2 films[59] at a high potential of 1.95 V (RHE) showed no catalyst corrosion whereas the thickness of anodically grown hydrous IrO_2 films decreases under similar conditions above 1.56 V (RHE).[59, 69] Polarisation at 1.6 V (RHE) has been observed to remove anodically grown oxide layers completely within 24 h.[63, 69]

In the light of the reviewed results, RuO_2 represents the best single-metal oxide catalyst known for PEWE applications if only activity parameters are considered. Its major disadvantage is the low stability which would result in very poor service lifetimes of PEWEs. A little inferior in activity, IrO_2 provides a better alternative because of higher stability. However, low availability of Ir does not allow large-scale production at reasonable costs. To tackle this issue, recent investigations focused on increasing the utilisation per unit mass of the employed noble metal. By scaling down the size of noble metal crystalline particles into the range of few nanometers, the surface area to volume ratio is enhanced. However, only few systematic investigations on the influence of catalyst particle size on the OER activity have been carried out so far.[51]

A different strategy to improve catalyst utilisation is to disperse the noble metal catalysts on high surface area non-noble supports. For instance, Wu and Scott[70] placed RuO_2 on Sb-doped SnO_2 nanoparticles and measured a higher activity than on unsupported RuO_2. Similar improvements have been achieved with supported IrO_2.[71] Three-dimensional substrate arrays of conductive tin doped indium oxide (ITO) showed high specific surface areas of 180 m^2/g. Employed as a support for IrO_2, the catalytic activity was increased compared to unsupported IrO_2. The introduction of tin doped indium phosphates as a replacement for the proton conducting Nafion® at the three phase boundary resulted in higher performances of the electrolysis cell.[71, 72]

Another option to achieve a stable and cost-effective catalyst is the partial replacement of noble with base metals by

either alloying or direct preparation of mixed oxides. The results of these investigations are discussed in the next sections.

3.2 Bimetal (oxide) electrocatalysts

The idea of synthesising binary metal oxide catalysts is based on the expectancy that the "advantageous properties of both components" can be combined within one material.[68]

A widely investigated bimetallic system is based on Ru and Ir with the aim of combining the very good catalytic activity of ruthenium oxide and the high electrochemical stability of iridium oxide. $RuIrO_2$ catalysts with 50% nominal Ir content prepared by thermal decomposition on Ti substrates show activities which are between those of pure RuO_2 and IrO_2 prepared by the same method. However, stability was not elucidated in this work.[46] On sputtered $Ru_xIr_{1-x}O_2$ Kötz and Stucki[68] identified a gradual change of Tafel slope and onset potential with composition x between the individual single metal-oxide values. Small additions of IrO_2 to RuO_2 reduced the galvanostatic corrosion rate significantly. An optimal trade-off of stability and activity is found for $0.5 < x < 0.8$. Ru-Ir alloys were also investigated by the same authors.[73] Similar to their results on sputtered mixed oxides, the alloy shows a gradually increasing Tafel slope and onset potential with the increase of the Ir content. Formation of an Ir-enriched oxide surface has been observed at potentials above 0.9 V (SCE, ~ 1.2 V vs. RHE) only on the alloy.

Furthermore, various other binary oxides have been investigated to either reduce corrosion of RuO_2 or decrease the amount of employed Ir while keeping the good catalytic properties of both materials.

In case of RuO_2, the introduction of a second metal cation in the structure aimed on improving the chemical stability of RuO_2 without impairing its OER activity. A thermally decomposed metal-oxide composition of Ru and Ta with a content of 50 mol% Ta shows a similar Tafel slope as RuO_2 in the range between 10^{-2} and 10^{2} μAcm^{-2} but a lower exchange current density.[46] A series of binary Pt-Ru catalysts shows a decrease in the mass current density while increasing the Pt content.[74] Differently the binary $Ru_{60}Co_{40}$ catalyst shows an almost double mass current density compared to a pure Ru catalyst.[75] The electrochemical stability and activity of nanocrystalline $Ru_xSn_{1-x}O_2$ powder catalysts as anode catalysts in a PEWE system revealed that addition of up to 40 mol% Sn even improved catalytic activity of RuO_2 synthesised by the same method.[70] A recent publication has claimed that Co and Ni incorporation into the RuO_2 structure can significantly improve the OER activity of the single material by activating a proton donor/acceptor functionality on the RuO_2 inactive surface sites.[76] As previously discussed, DFT calculations have revealed a linear relationship between the binding energy of the reaction intermediates, resulting in an inevitable OER overpotential of about 0.4 V (see **Figure 8**).[18] However, Ni and Co-doped RuO_2 catalysts seem to overcome the activity volcano plot limitations, as shown in **Figure 8**.[76] According to the author's model, the small overpotential for Ni and Co-doped RuO_2 could be

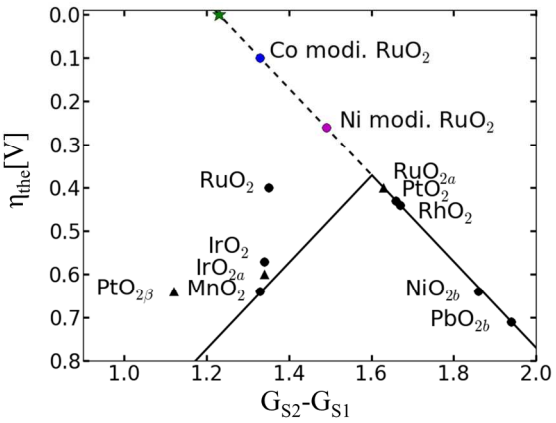

Figure 8 Updated Volcano plot shown in **Figure 5** with the overpotential of Ni and Co modified RuO_2. The activation of bridges sites by Ni and Co incorporation into RuO_2 breaks the scaling relationship between the binding energy of reaction intermediates. The green star marks the position of an ideal catalyst. Reproduced from Ref. [76] with permission from the PCCP Owner Societies.

achieved by modifying a bi-dimensional active site into a three-dimensional one. Typically, the active sites are confined to the surface metal cations which form *n-1* oxygen bonds (where *n* is the number of oxygen bonds for the same cation in the bulk). These reaction sites can be modified by the introduction of a heterovalent cation like Co or Ni able to activate "bridge" sites.[76] However it should be remarked that besides an academic interest in overcoming previous theoretical limitations, the corrosion stability of Co and Ni-containing catalysts should be verified in order to assess possible cation dissolution.

Regarding IrO_2, most of the research efforts have been oriented towards enhancing the catalytic activity or in reducing the amount of Ir in the catalysts without affecting the catalytic activity. De Pauli and Trasatti studied the activity and stability of Ir-Sn mixed oxides thermally prepared on Ti substrates.[77] Tafel slopes similar to those of pure IrO_2 films have been observed decreasing the Ir content down to 10 mol%. Additional studies on Sn-Ir oxides have been carried out by Marshall et al.,[78] which showed that contents up to 20 mol% of Sn in IrO_2 have no significant influence on the activity determined in an aqueous acidic electrolyte. However, further galvanostatic investigations of anodic $Ir_xSn_{1-x}O_2$ powder catalysts in a PEWE cell setup performed by the same authors showed a performance reduction even upon small additions of Sn. [78] A recent work demonstrates the viability of "metal–oxide hybrid core–shell" nanoparticle catalysts formed through a dealloying and a selective oxidation procedure.[79] Core-shell nanoparticles with a NiIr core supporting a shell of IrOx catalyst show a 3-fold catalytic activity enhancement compared to Ir. The enhancement in mass activity was attributed to (i) an increase of the electrochemical active surface area of the catalyst during the selective dealloying, (ii) electronic and strain effects resulting from the presence of a Ni-containing core, and (iii) the reduction of the Ir content due to the Ni-based core.

The latter studies show that the introduction of a non-noble metal element can help improving stability and reducing catalyst cost without affecting the catalytic activity to an unreason-

able extent. Additionally to this strategy, the interfacial area between catalyst and electrolyte can be increased by using high area supports as in the case of single metal catalysts. Binary mixed oxide nanoparticles containing RuO_2 and IrO_2 dispersed on antimony doped tin oxides achieved similar performances as thin film electrodes of the same type but with a reduced loading of noble metals.[80]

A different, recent approach to enhance catalytic activity of the Ir catalyst was taken by Kadakia et al.[81] who synthesised fluorine doped IrO_2 thin films. These films showed a significant increase in activity relative to pure IrO_2 at dopant contents around 20 wt%. Furthermore, the onset potential of oxygen evolution was not affected by the amount of fluorine introduced. Theoretical attempts to describe the advancing effect of fluorine point to a decrease in the difference of Gibbs energy of the rate determining step[82] based on the argumentation of Man et al.[18] and described in the previous section. Similar ideas have been applied to $Sn_{0.8}Ru_{0.2}O_2$.[83] While doping $Sn_{0.8}Ru_{0.2}O_2$ with 10 wt% of fluorine allowed achieving activity similar to the one of RuO_2, only minor advances were achieved on the subject of stability.

In order to increase stability and to probably enhance synergetic effects, different ternary additives were introduced into the bimetallic catalyst systems. These ternary oxide catalysts are discussed in the next section.

3.3 Ternary and multimetallic oxides

Even though incorporation of Ir into Ru-oxides can improve the stability of the latter catalyst, ternary Sn-Ir-Ru-oxides show a further improved durability.[84] Galvanostatic activity assessment of crystalline $Ir_xRu_{0.5-x}Sn_{0.5}O_2$ powders within a PEWE system revealed that oxides with $0.25 < x < 0.35$ show a similar performance as pure IrO_2 electrodes concomitant with a decrease in overall catalyst costs.[80]

The thermally prepared ternary mixed oxides $Ru_{0.5}Ir_{0.5}TaO_x$ and $RuIr_{0.5}Ta_{0.5}O_x$ exhibited lower Tafel slopes and higher exchange current densities than identically synthesised RuO_x.[46] Higher stability under galvanostatic conditions have been reported for both oxides compared to RuO_x. Nevertheless, more recent performance tests in PEWE water electrolysis cells employing $Ir_xRu_yTa_zO_2$ as the anode catalyst showed higher overpotential with increased Ta content within the range of applicable current densities.[85]

Boodts and Trasatti performed potentiodynamic investigations to elucidate activity parameters of $Ru_{0.3}Ti_{0.7-x}Sn_xO_2$ for different compositions.[86] Enhancement of activity with increasing Sn content was observed while the Tafel slope and reaction order were independent of composition and represented the value of Ru. Differences in stability relating to the Ti/Sn ratio were not explicitly identified. Replacement of Ti with Pt in $Ir_{0.3}Ti_{0.7-x}Pt_xO_2$ ternary oxides resulted in an increase of Tafel slope and ohmic layer resistance.[87] The activity decreases with higher Pt content.

4 Catalyst materials for alkaline water electrolysers (AWEs)

Alkaline water electrolysers (AWEs) were the first low temperature fuel cell developed in the 1960s and mainly used for space program applications. Afterwards, mostly due to the liquid electrolyte deterioration in contact with CO_2, the interest in these systems has been shelved for many years. However, overcoming the previous limiting drawback of electrolyte carbonization by using a polymeric anion conductive membrane,[88] the interest in AFCs has risen again in the recent years. IrO_2 and RuO_2 are excellent catalysts also for AWE applications. However, in AWEs the use of an electrolyte with a high pH value provides the advantage that several base metals show adequate corrosion stability in alkaline environment. Therefore, a wide range of catalyst materials alternative to IrO_2 and RuO_2 can be investigated. The possible replacement of noble metals catalysts with low-cost and abundant transition metal based oxides represents one of the major advantages of AWE devices compared to PEWEs since it allows cost reduction facilitating a widespread market penetration. However it should be also mentioned that AWEs present generally lower voltage efficiencies at high current densities compared to PEWEs. In addition, traditional AWEs are not capable to be operated above 50 bar, so high pressure operation as in the case of PEWEs is not applicable. This issue, however, may be overcome by alkaline membrane electrolyser systems, which in principle may be operated at p >30 bar.[89]

Regarding OER catalysts materials for AWEs, the most promising transition can be found in the fourth row of the periodic table (the so called *3d* elements), especially Mn, Fe, Co and Ni. Among them, the most accepted catalytic activity trend is reported as Ni > Co > Fe > Mn, as shown in **Figure 9**.[90]

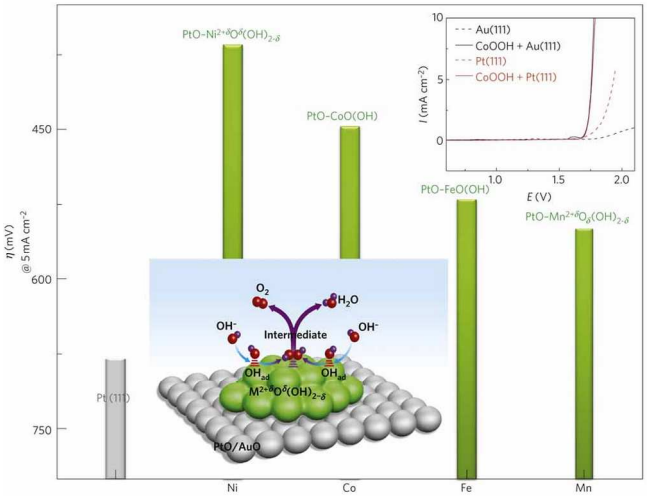

Figure 9 Reactivity trends (overpotential in mV at 5 $mAcm^{-2}$) for the OER on 3d-metal hydr(oxy)oxide clusters deposited on Pt(111) surfaces. Top inset: a comparison of polarization curves for Pt(111) , Au(111), CoOOH on Pt(111), and CoOOH on Au(111). Reproduced with permission of ref. [90].

Besides binary oxides, also perovskites have recently attracted significant attention as potential catalysts for the OER. The topic of this chapter will be focused in reviewing the catalytic activities of transition metal based catalysts for application in AWE devices. As already mentioned for PEWE catalysts, due to the high oxygen evolution overpotentials most of the metal catalysts present an oxidised surface layer during operation. Therefore in the following all the oxygen evolution catalysts will be presented as oxides.

As already discussed for IrO_2 and RuO_2 catalysts in the previous sections, also for most of the AWE catalysts materials the activity depends on the processing and electrochemical pretreatments of the catalyst.[91, 92] In the early 1980th, Iwakura et al.[93] already indicated an effect of the substrate material on the OER overpotential of cobalt catalysts if an annealing step at high temperatures (in this case at 350 °C) was part of the synthesis route. The heat treatment led to a diffusion of the substrate atoms into the cobalt oxide top layer, influencing its catalytic properties. Yeo et al.[94] have recently suggested a further possible interaction between the substrate and the catalyst material. They investigated the catalytic activity of few monolayers of cobalt oxide galvanostatically deposited on different metal substrates, observing a decrease in the TOF as a function of the substrate material in the order Au > Pt > Pd > Cu > Co. In the authors model, the activity towards the OER is enhanced when the catalyst is in a higher oxidation state (here Co(IV) instead of Co(III)) since this might lead to a nucleophilic influence of the catalyst active site on incoming OH. They further suggested that more electronegative substrates, such as Au, might act as an electron sink facilitating the oxidation of the catalyst layer on top of it. However, the influence of the substrate on the OER activity could be only observed for few monolayer of the deposited catalyst. In a different study no influence on the OER activity of several transition metal (Ni, Co, Fe, Mn) oxide clusters has been observed using Pt(111) or Au(111) substrates (top inset of **Figure 9**).[90] The discrepancy between the latter studies might come from the use of different catalyst loadings/microstructures, i.e. only for low catalyst loadings the substrate might have a significant influence on the catalyst OER activity.

It is worth mentioning that besides a possible influence of the substrate on the OER activity, in several studies the catalyst material has been mixed with carbon[95-97] or supported on nickel.[98, 99] Carbon can be thermodynamically oxidised at a potential as low as 0.207 V (RHE).[100] Due to kinetic hindrances, carbon undergoes a strong corrosion above 1.1 V (RHE). Therefore in the typical operating potentials for the OER it is expected that carbon will be strongly corroded during operation. As a consequence, a high anodic current not only due to OER would be observed during experimental measurements. Besides carbon, also the use of a Ni substrate should be avoided since, as it will be described in details below, Ni has high activity towards the OER. Some studies have also shown that iron contamination caused by impurities in the KOH electrolyte can have an influence on the experimentally measured OER activity.[101, 102] Particularly with regards to the described high OER activity of iron doped nickel, an influence of the iron on the reported catalytic performances cannot be ruled out. Other electrochemical OER measurements were carried out in nitrogen saturated electrolyte, which leads to a shift of the OER equilibrium potential during initial oxygen evolution. Last but not least, the methods for real surface area determination of the catalyst vary a lot between different studies. Therefore a comparison of charge densities is proving difficult.

4.1 Nickel-based oxides

Nickel is one of the most promising transition metal catalysts for the OER in alkaline media. Metallic nickel immersed in an aqueous solution at open circuit potential instantaneously forms a layer of $Ni(OH)_2$ on top of the air-formed NiO layer. The Ni hydroxide layer grows upon continuous potential cycling across the $Ni(OH)_2$/NiOOH redox peak.[103] Furthermore, the studies of Medway et al.[104] on single crystal Ni(111) indicate that both the first NiO and the topmost $Ni(OH)_2$ layers grow during potential cycling as illustrated in the sketch in **Figure 10** (upper panel). Upon the growth of the $Ni(OH)_2$ layer a significant increase in the OER activity is generally observed, as shown in **Figure 10** (lower panel) for a hydrous nickel oxide film.[105] The shift to more anodic potentials for the anodic Ni(II/III) peak[105] in **Figure 10** (lower panel) suggests the formation of a more thermodynamically stable $Ni(OH)_2$ phase and a less reversible behaviour of the surface redox couple. Fundamental understanding of the $Ni(OH)_2$/NiOOH redox couple was provided by Bode et al.[106-108] who suggested the existence of two limiting discharged phases, the α-$Ni(OH)_2$ and the β-$Ni(OH)_2$ phase, and two limiting charged phases, γ-NiOOH and β-NiOOH. The α-$Ni(OH)_2$ phase (oxidation state 2.0–2.2) is significantly hydrated, poorly crystalline, and upon increasing the electrode potential can be oxidised to the γ-NiOOH (oxidation state 3.5–3.67). The β-$Ni(OH)_2$ phase (oxidation state 2.0–2.2) is largely anhydrous and crystalline, and it can be oxidised to β-NiOOH (oxidation state 2.7–3.0).[103, 104, 109] Several authors[110, 111] proposed that an initially formed α-$Ni(OH)_2$ phase could gradually change into a more crystalline β-$Ni(OH)_2$ phase due to potential cycling in a strong base. It has been also suggested that the β-$Ni(OH)_2$ phase is the most active for the OER since its oxidation to the β-NiOOH phase represent the optimal condition for the OER to occur.[109, 112, 113] Besides the creation of an optimal $Ni(OH)_2$ layer upon potential cycling, the latter can also increase the surface roughness and the amount of the electrochemically active surface area, then leading to a larger oxygen evolution activity.[114] Since the thickness of the $Ni(OH)_2$ layer is time dependent [104, 115] and it can present different physical and morphological properties, the activity of nickel based electrodes depends strongly on their history (synthesis and potential cycling).[92] Indeed, a huge spectrum of Tafel slopes, varying from about 40 to 130 mV/dec, can be found in the literature.[92, 101, 103, 105, 116-119] Several studies indicate that independently on the material processing two regions for the Tafel slope can be identified, with a change in the Tafel slope value at about 1.5 V (RHE).[92, 101, 103, 116]

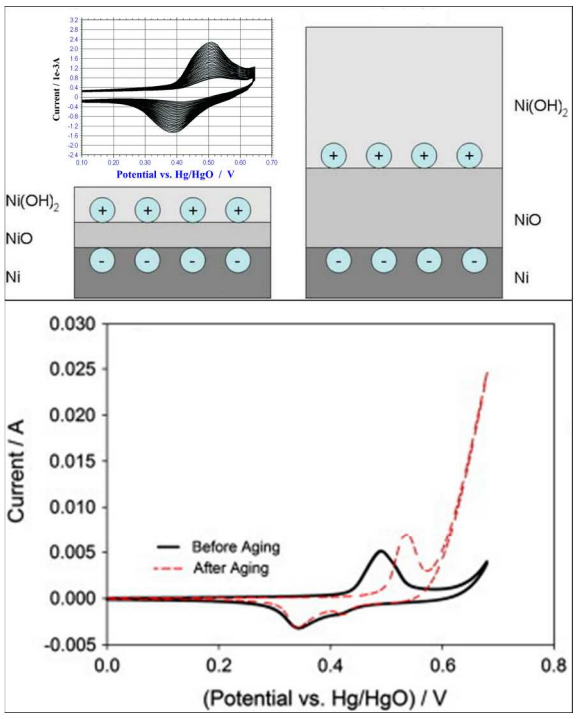

Figure 10 The upper panel shows a schematic diagram of the growth of the oxidic layers by cycling single crystals Ni(111) across the $Ni(OH)_2$/NiOOH voltammetric peaks. Reproduced with permisiion of ref. [104]. In the inset the Ni hydroxide/oxyhydroxide voltammetric redox couple are also shown. Reproduced by permission of The Electrochemical Society.[103] The lower panel shows the increase of the OER activity for a hydrous nickel oxide film after potential cycling across the $Ni(OH)_2$/NiOOH redox peaks. Reproduced with permission of ref. [105].

In order to improve the catalytic performance of nickel electrodes, numerous studies dealt with doped nickel, using transition metals as dopants in a wide range of compositions. Like already mentioned, the electrocatalytic activities of nickel and its alloys depends on their history, e.g. the synthesis route,[119] hence influences of the doping concentrations can only be described among samples synthesised identically. Additionally it should be noted that the determined surface area depends strongly on the measuring technique. It is therefore difficult to compare absolute values of surface areas and current densities respectively measured with different techniques. Li et al.[120] have investigated a wide range of doped nickel-based catalysts prepared by electrodeposition of metallic salts on nickel microelectrodes. In **Figure 11** the polarisation curves of nickel oxide mixed with various first row transition metals are shown. According to the authors, iron is the most promising alloy element for enhanced catalytic activity of nickel-based OER catalysts. This conclusion matches with the indication of several other studies. Corrigan[101] and Merrill et al.[121] reported Tafel slopes for NiFe oxides as little as 17 and 14.8 mV/dec respectively. Other studies[101, 118] showed that already around one percent of iron doping has strong influence on the catalytic activity of electrodeposited and sputtered nickel oxide films. Particularly, for about 5 mol% of iron a decrease of 50-60 mV/dec and 140-160 mV for the Tafel slope and the OER overpotential (taken at 8 mA/cm^2), respectively, was observed.[101, 118] The latter results demonstrated that small amounts of iron impurities can have a significant influence on the activity of nickel based catalysts. Therefore, for a true understanding of the nickel electrocatalytic activity the use of high purity electrolytes and a clean environment is mandatory. Additionally, given the high sensibility of the material to metal impurities, the surface chemical composition after the electrochemical measurements should be determined. Consideration of both of the mentioned points, however, are strongly lacking in the studies provided in the literature so far.

The best doping concentration of Fe is indicated quite controversial in the literature. While some studies report the best OER activity at a doping concentration of about 10 mol % Fe,[101, 120, 122] other authors claimed that the lowest Tafel slope[117] or the smaller overpotential[123] can be obtained doping Ni with 40 mol% of Fe. Also the mechanism leading to superior OER activity for Ni/Fe catalysts is still rather unclear. Smith et al.[117] indicated that iron as an alloying element stabilises the higher oxidation states of nickel, leading to a superior OER activity. Differently, Louie and Bell[123] claimed that Fe incorporation into Ni increases the potential at which $Ni(OH)_2$/NiOOH redox reaction occurs and decreases the average oxidation state of Ni in NiOOH.

Besides the introduction of a second transition metal into the Ni structure, the catalytic activity can be also improved by using tailored morphologies. A simple way of increasing the mass specific activity is by increasing the catalytic active surface area of a catalyst. For example, Xu et al.[124] synthesised NiOOH in a 3D-flowerlike morphology with large surface area, as shown in **Figure 12**.

As already discussed, the wettability of the electrode plays a decisive role for the electrolyser efficiency. At high currents, gas bubbles formed at the electrodes are responsible for high ohmic losses. Recently, Ahn et al.[125] showed by a simple experiment that the detachment of gas bubbles and consequently the efficiency of an electrolyser can be significantly enhanced by increasing the surface roughness of the nickel anode.

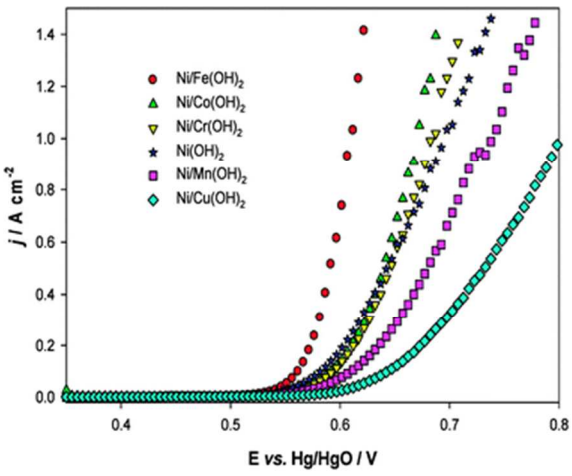

Figure 11 Steady state polarisation curves recorded for various coatings on a Ni microdisc electrode in 1 M NaOH at 80 °C. Potential sweep rate: 1 mV/s. Reproduced from Ref. [120] with permission from the PCCP Owner Societies.

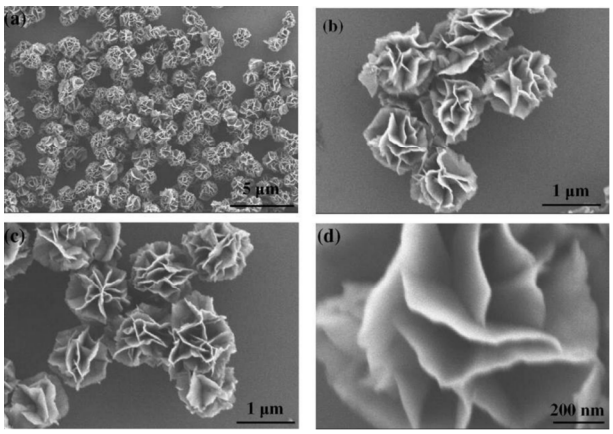

Figure 12 Field-emission scanning electron microscopy images of α-Ni(OH)$_2$ with a 3D-flowerlike morphology at different magnifications. Reproduced with permission of ref. [124].

4.2 Cobalt-based oxides

Another promising transition metal catalyst is cobalt. Smith et al.[117] observed an overpotential of 0.26 V at 0.5 mA/cm² for the OER on undoped amorphous cobalt. Like nickel, cobalt gets oxidised when inserted in an aqueous electrolyte. Under anodic potential cobalt undergoes several oxidation steps before oxygen evolution sets in. During that process, a layered structure of oxidic cobalt species is formed when Co(II) gets gradually oxidised to Co(III).[91, 94] Some authors even reported the formation of Co(IV) species on the outer surface of the electrode.[91, 126, 127] The catalytic activity of cobalt depends on the oxide composition and on the electrochemical pre-treatment of the metal electrode.[91] The OER generally shows two overpotential regions[9, 91, 128-130] with different Tafel slopes, being the most reported slope at low overpotentials 42 mV/dec.[91, 102, 117, 128, 129, 131, 132]

As it was already indicated in the early 1980s by Iwakura et al.[93], the catalytic activity of cobalt can be enhanced forming solid solutions with other transition metals. Recently, Bajdich et al.[133] calculated the overpotentials for the OER on two different crystallographic surfaces of CoOOH (**Figure 13**). They found that the thermodynamically stable crystallographic surfaces of CoOOH under OER conditions depend on the applied potential and pH value, according to:

$$U_t = 1.9\ V - 0.059\ V \times pH \qquad (8)$$

Particularly, for alkaline media (pH ≈ 13) the transition potential U_t is about 1.13 V. Below this potential, the Co(10$\underline{1}$4) surface is the most stable (**Figure 13**, upper panel), while above 1.13 V, the Co(01$\underline{1}$2) surface is predominant (**Figure 13**, lower panel). From the DFT calculations, the most promising dopants appear to be Ni and V for the Co(10$\underline{1}$4) surface and the Co(01$\underline{1}$2) surface, respectively. Particularly, for long term applications at high anodic potentials (where the Co(01$\underline{1}$2) surface is predominant) vanadium could represent a quite promising dopant for cobalt oxide.

Experimental studies on the influence of nickel as doping element are at present quite contradictory: On one hand, Trotochaud et al.[102] compared the catalytic activity of nickel, cobalt and their alloys and reported an enhanced electrocatalytic activity of the alloy catalysts. They observed a decrease in the Tafel slope (from 42 to 29 mV/dec) and in the overpotential (from 381 to 300 mV at 1 mA/cm^2) with an increasing fraction of nickel $Ni_xCo_{1-x}Oy$ ($0 \le x \le 1$). However, Fe contamination was observed by the authors, potentially affecting their results. On the other hand, Smith et al.[117] reported a decreased catalytic activity of cobalt if alloyed with nickel: alloying Co with 59 % nickel the Tafel slope increased from 42 to 73 mV/dec while the overpotential was almost constant.

Numerous research studies deal with copper doped cobalt oxides. According to the findings of the DFT calculations of Bajdich et al.[133] shown in **Figure 13**, the catalytic OER activity of cobalt oxide would decrease with increasing amount of copper. Contrary to those findings, other studies have reported an increase in activity due to copper doping, indicating different optimal compositions ($CuCo_2O_4$,[134]; $Cu_{0.7}Co_{2.3}O_4$,[135]; $Cu_{0.3}Co_{2.7}O_4$,[99]). Like mentioned in the introduction, besides the catalytic activity, the electrical resistivity and especially the long term stability are of high interest for applications. Jia et al.[136] observed a large decrease in the electrical resistivity for for Cu-doped cobalt oxide, reaching the minimum for the $Cu_{0.3}Co_{2.7}O_4$, composition. Contradictory results towards the trend of the long term stability of $Cu_xCo_{3-x}O_4$ were observed: While Jia et al.[136] and Wu et al.[135] reported an increased

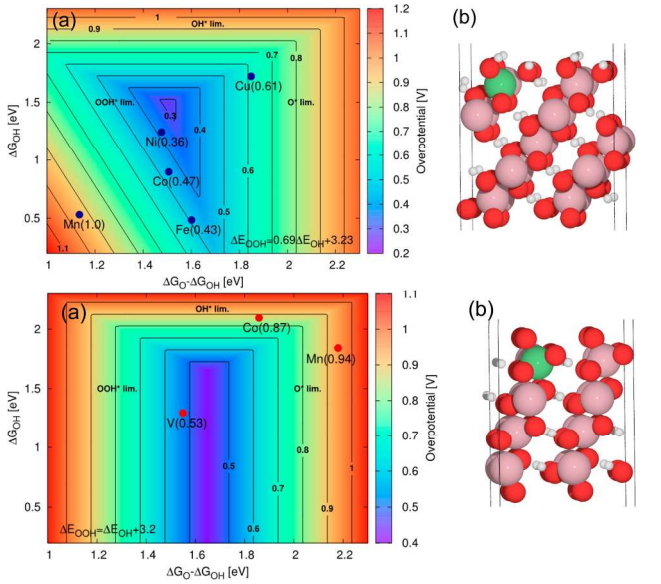

Figure 13 (a) 2D map of theoretical overpotentials η for the doped (10$\bar{1}$4) surface (upper panel) and for the (01$\bar{1}$2) surface (lower panel) of β-CoOOH as function of $\Delta G_O - \Delta G_{OH}$ and ΔG_{OH}. The individual values of η are indicated in brackets. The contour map is constructed assuming $\Delta E_{OOH} = E_{OH} + 3.2$ eV. For the (10$\bar{1}$4) surface (upper panel) improvement in activity relative to undoped surface is obtained in the case of Ni with η = 0.36 V and Fe with η = 0.43 V. For the (01$\bar{1}$2) surface (lower panel) the improvement relative to undoped surface is obtained in the case of vanadium with η = 0.53 V. Only the dopants with η < 1 V are shown. (b) The corresponding atomic system with the green sphere indicating a position of the dopant. Reproduced with permission of ref.[133].

corrosion stability of $Cu_{0.3}Co_{2.7}O_4$ compared to undoped Co_3O_4, Berenguer et al.[137] reported a higher susceptibility for corrosion increasing the copper content. However different protocol were used to test the stability of the catalyst materials: While Jia and coworkers[136] employed the electrode periodically as both anode and cathode, Berenguer and coworkers[137] applied anodic potentials to achieve a constant current density of 100 mA/cm^2.

With the aim of taking advantage of both nickel and copper as alloy elements, Wen et al.[138] systematically investigated ternary Co-Ni-Cu alloys, showing that the highest current densities at an overpotential of 700 mV can be achieved with ternary alloys of 50-63 % Co, 30-40 % Ni and 5-15 % Cu (**Figure 14**). The catalytic activity of ternary cobalt alloys different from Co-Ni-Cu were also investigated. For example, Rosalbino et al.[139] prepared ternary $Ni_{60}Co_{30}M_{10}$ (M = Cr, Mn, Co, Cu) alloys and compared their catalytic OER activity. They observed decreased Tafel slopes and overpotentials in order of enhanced activity: $Ni_{60}Co_{30}Cr_{10}$ > $Ni_{60}Co_{30}Mn_{10}$ > $Ni_{60}Co_{30}Cu_{10}$ > $Ni_{60}Co_{40}$. Lee et al.[140] investigated ternary Co-Cu-Zn oxides. The maximum activity they found for 70 to 85 % Co, 10 to 20 % Cu, and 2 to 10 % Zn. Besides nickel and copper, various other transition metals were investigated as additives for cobalt oxide catalysts. However no significant improvement in the catalytic activity has been reported, to the best of our knowledge. For example, Rios et al.[141] systematicallyinvestigated $Mn_xCo_{(3-x)}O_4$ ($0 \le x \le 1$) spinel films and observed a slightly decreasing activity with increasing content of manganese as the Tafel slope did almost not change while the current density decreased monotonically at fixed potential.

Some studies deal also with carbon supported Co-based catalysts, e.g. $NiCo_2O_4$.[97] Even though an increase in performance was observed when $NiCo_2O_4$ was mixed with carbon, we cannot rule out that the increase in activity is simply due to additional carbon oxidation currents. Indeed, as mentioned above, carbon is not stable at high anodic potentials and a high corrosion rate is expected.

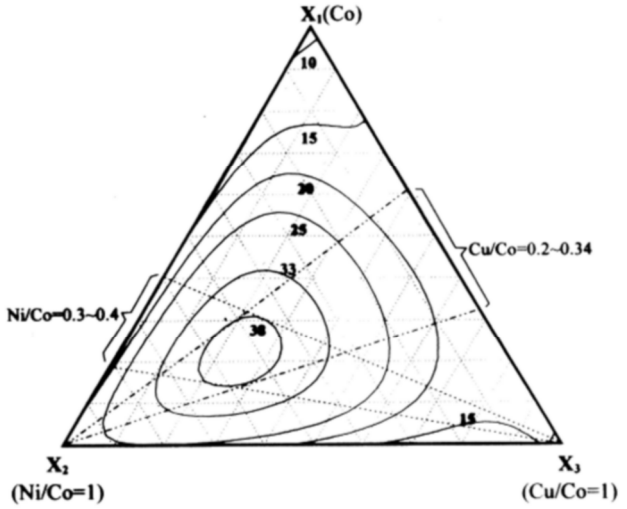

Figure 14 A plot of oxygen evolution activity vs. coating solution composition for Co–Ni–Cu ternary electrodes. The numbers associated with contour lines represent current density (mA/cm^2) results. Reproduced with permission of ref.[138]

4.3 Other transition metal based oxides

As already mentioned, other *3d* elements than Ni and Co can show a reasonable catalytic activity towards the OER. Several studies on transition metals such as Fe or Mn-based oxides have been published so far. Unfortunately, most of the published work is based on data obtained using a nickel support or by adding carbon species to the catalyst. Like already mentioned, nickel shows high catalytic activity and carbon oxidises very fast at high potentials; therefore their use as supports makes the evaluation of the catalytic activity unreliable.

IRON-BASED. Joiret et al.[142] investigated the Fe surface oxidation as a function of the applied potential by in situ Raman spectroscopy; below -0.9 V (Hg/HgO) Fe_3O_4 (Magnetite) was observed, gradually converting into α-FeOOH above -0.53 V (Hg/HgO). At more anodic potentials Fe_3O_4 changes to γ-FeOOH and γ-Fe_2O_3 at the surface. In the bulk, at any investigated potentials, Fe_3O_4 was found. For single Fe oxide catalyst Smith et al.[117] reported a Tafel slope of 40 ± 4 mV/dec and an overpotential for the OER of 0.38 V at a current density of 0.5 mA/cm^2. Singh et al.[98] investigated nickel supported $CoFe_{2-x}Cr_xO_4$ ($0 \le x \le 1$) electrodes, showing a maximum activity for $CoFe_{1.2}Cr_{0.8}O_4$, with a Tafel slope of 40 mV/dec and an overpotential of 615 ± 4 mV at a current density of 100 mA/cm^2. The same compositions were investigated by the authors with a platinum support a few years later again. In that case they observed an overall trend of increasing OER activity with increasing Cr content.

MANGANESE-BASED. Messaoudi et al.[143] investigated the Mn oxidation state as a function of the applied potential by in situ Raman spectroscopy. At very cathodic potentials (below ~ 0.5 V RHE), Mn_3O_4 (Hausmannite) was observed, while above ~ 0.9 V RHE the formation of a phase similar to Mn_2O_3 (Bixbyte) occurred. The latter transformed into MnO_2 (Ramsdellite) at potentials above ~ 1.4 V RHE. At potentials above ~ 1.7 V RHE the formation of MnO_4^- was observed by a colour change of the electrolyte to violet. A relatively high Tafel slope of about 110 mV/dec was observed for manganese oxide above roughly 100 mA/cm^2.[144, 145] Recently, further insights into structure–activity relationships for manganese based catalysts have been provided.[146, 147] Bergmann et al.[147] by developing a layered and 3D crosslinked MnO_x catalyst structure showed that the presence of di-m-oxo-bridged Mn ions in the layered structure results in a pronounced redox and charge capacity behavior but a relatively large Tafel slope. Differently, the 3D cross-linked structures with both mono- and di-m-oxo-bridged Mn ions present lower intrinsic OER activity but smaller Tafel slope.

Besides for the application in "dark" electrolysis, manganates and calcium manganates are widely investigated as anode material as photocatalysts for water splitting.[148, 149]

4.4 Perovskites

The basic perovskite structure can be represented as ABO_3, where A is the larger cation, such as a lanthanide or an alkaline earth element, and B is the smaller cation, generally a transition

metal surrounded by 6 oxygen atoms forming a BO_6 octahedral (**Figure 15**). The ABO_3 structure can accommodate cation substitution in a wide range by partial replacement of both the A and the B cation with another element giving $(A_xA`_{1-x})(B_yB`_{1-y})O_3$ compositions. Such substitution leads to modification of the perovskite band structure which in turn can modify the electrical, optical and magnetic properties of the oxides, and, thus, may also have a significant effect on their catalytic activity. In most cases the outer orbitals of the A ions do not play an important role in determining the perovskite electronic properties, which can be regarded as arising solely from the BO_6 octahedral. This is not to say that the A ion is not important. The electrostatic potential of the A ion influences the energy of the conduction band, and its size determines a possible deviation of the crystal structure from the ideal cubic form. When the B cation is a transition metal, the outer s and p orbitals form a filled valence band and an empty conduction band separated by a large energy gap; thus, they contribute only little to the material physical properties. The electrons of interest for the conduction properties are the d-band electrons (d-band perovskites).[150]

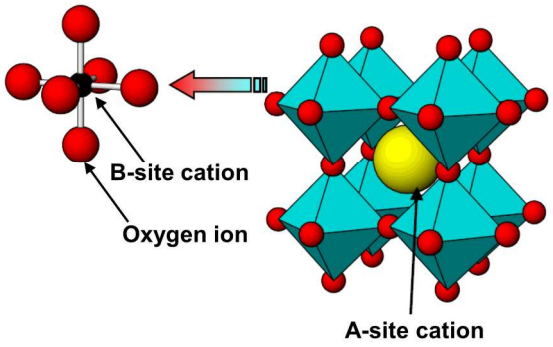

Figure 15 Sketch of a basic ABO_3 basic perovskite oxide structure.

The first literature correlating perovskite band structure and their catalytic activity toward oxygen electrocatalysis goes back to the end of the 1970s. Matsumoto et al.[151] initially proposed that the main parameters governing the OER at the surface of d-band perovskites are *(i)* the formation of a σ* band in the lattice which should enhance the electron transfer between the OH^- and the electrode surface and *(ii)* the oxidation state of the transition metal cation (B site). Furthermore, Matsumoto et al.[151] suggested that the OER proceeds on the surface of perovskite oxides following the so called Kasil'schikov path reported in **Table 2**. According to the authors, the rate of the 1st and 3rd reaction steps (both comprising an electron transfer) would be enhanced for those perovskites showing extended σ* band. Differently the chemical reaction step (2nd step) would be favoured in case of perovskites having the B site transition metal cation in a high oxidation state. The assumptions of the authors were partially supported by the study of $La_{1-x}Sr_xFe_{1-y}Co_yO_3$ perovskite series. Particularly they found that the oxygen evolution overpotential at a defined current density and the Tafel slope decreased with increasing x and y in the perovskite series, with the exception for $SrCoO_3$ and $SrFeO_3$ compounds. The calcined $SrCoO_3$ did not show a perovskite structure and exhibited high resistivity, which could explain the deviation from the above mentioned trend of oxygen evolution activity vs. the increase of x and y in $La_{1-x}Sr_xFe_{1-y}Co_yO_3$.

Theoretically, $SrCoO_3$ should possess the largest σ* band and also large amount of B-site cations in IV+ instead than in III+ or II+ oxidation state; these would represent the optimal properties of a superior perovskite oxygen evolution catalyst according to the theory of Matsumoto et al.[151] Interestingly, the DFT calculations performed by Man et al.[18] show a volcano relation between catalyst overpotential and intermediates adsorption energy with $SrCoO_3$ sitting on top of the volcano plot close to $LaNiO_3$ and $SrNiO_3$ (**Figure 5**).

It was reported by Otagawa and Bockris[152] that also $LaNiO_3$ displays excellent oxygen evolution activity with a Tafel slope of about 40 mV/s. The authors[153] suggested that the high activity of $LaNiO_3$ was due to weak bonding strength of the OH on the perovskite surface. In a following paper[15] Bockris and Otagawa further stressed the importance of the bonding strength of surface oxygenated intermediates on the oxygen evolution activity of perovskite oxides. They showed that for several $La_{1-x}A_xBO_3$ perovskites (**Figure 16**) the oxygen evolution activity increased with decreasing the B-OH bond strength from vanadium to nickel (B-site element) and with the increase of the number of d-electrons of the transition metal cations (considered in III+ oxidation state). Besides experimental data, these authors[15] also proposed (**Figure 16**) a volcano plot of activity vs. intermediates bonding strength similar to that predicted by DFT calculation in ref [18] and shown in **Figure 5**. According to Bockris and Otagawa[15] the linear scaling of the oxygen evolution activity either with the intermediate bond strength and the number of d-electrons occurs because the last two materials properties are interconnected. An important feature of the perovskite surface is that the BO_6 symmetry is broken and thus the electrostatic crystalline field results perturbed leading to further splitting of the e_g and t_{2g} bands. Furthermore, when the oxide surface is in contact with an aqueous solution, such as KOH, most of the oxides have an affinity for adsorption of OH-ions. The surface states have wave functions which can hybridise with the orbitals of the reacting molecules to produce a surface complex. Bockris and Otagawa,[15] taking into account a possible surface electronic configuration, proposed that the electrons from the d-orbitals of the surface transition metals will occupy the antibonding orbitals of B-OH molecular orbitals. Thus, the authors suggested that the B-OH bond strength would decrease as the number of d-electrons increases. It was also found that perovkites showing lower stability displayed higher activity.[15] The author used these results to remark that perovskites able to easily loose lattice oxygens and/or easily forming oxygen vacancies should display the lower bond strength with oxygenated species and, thus, the highest activity Also Trasatti[154] has pointed out that for different oxide materials a correlation between the degree of non-stoichiometry and the O_2 electrocatalytic activity exists. Bockris and Otagawa,[15] also tried to correlate the perovskite activity with other bulk

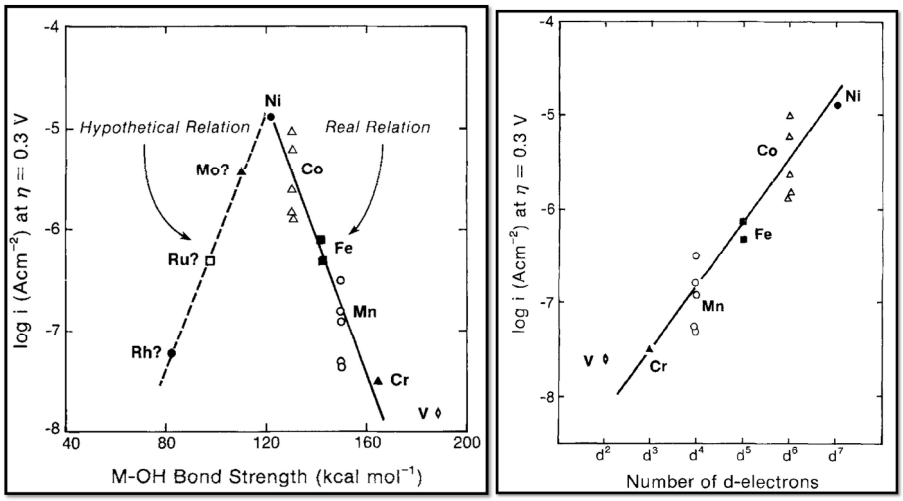

Figure 16 Left side, a hypothetical volcano plot for the oxygen evolution activity vs. the M-OH bond strength for $LaMO_3$ perovskites (M= Rh, Ru, Mo, Ni, Co, Fe, Mn, Cr, V). Right sie, activity vs. number of d-electrons for different B-site transition metal ions in $LaMO_3$ perovskites (M= Ni, Co, Fe, Mn, Cr, V). Reproduced by permission of The Electrochemical Society.[15]

properties typical for semiconducting materials, such as flat band potential, carrier density, and Hall mobility; however, an univocal correlation was not found. The reaction mechanism for the OER on the perovskite surface proposed by Bockris and Otagawais is also reported in **Table 2** (Brockis path). [15, 153] Basically, the water molecule, originally adsorbed on a reaction site S, can be replaced by an OH^- by a proton transfer. Hence, an electron transfer may occur. For a wide range of perovskites, the authors indicated as the RDS the electrochemical desorption of OH. In case of $LaNiO_3$ they proposed that given the high oxygen vacancy concentration in the perovskite lattice (i.e. lattice oxygen loosely bound), the oxygen evolution may take place with direct participation of the surface lattice oxygens in the form of OH^- ions.[153]

After a wide time gap, a growing number of publications on perovskite oxides for application as oxygen evolution catalysts have appeared in the last couples of years. To design superior catalysts descriptors, Suntivich et al.[155] also applied an approach based on orbital principles; they reported a volcano plot correlation between the oxygen evolution activity of different perovskites with the e_g filling. They suggested that not the whole d-band occupation influences the binding energy of surface oxygenated species but only the e_g occupancy, which can be therefore used as descriptor for the oxygen evolution activity. They identified $Ba_{0.5}Sr_{0.5}Co_{0.8}Fe_{0.2}O_{3-\delta}$ (BSCF) perovskite as the most promising oxygen evolution catalyst. BSCF sits on top of the volcano plot of activity vs. e_g filling,[155] differently from the volcano plot reported in **Figure 5** for perovskites where $SrCoO_3$ and $LaNiO_3$ are identified as the best oxygen evolution catalysts (however different perovskite compositions were considered in the two studies).

Besides the earlier investigation on $LaNiO_3$,[152] more recently Hardin et al.[156] showed a high mass activity for composite electrodes made of $LaNiO_3$ nanoparticles and N-doped carbon nanotubes, suggesting the direct participation of lattice hydroxide species in the OER similar as proposed in ref. [[152]].

While in the latter paper[156] it is clearly specified that carbon addition allows increasing the measured anodic current, most of the recent papers on perovskite catalysts include carbon in the electrode composition without checking its influence on the oxygen evolution activity.[155-159] However, it has been recently shown for the BSCF catalyst that carbon addition results in an increase of anodic current for the composite electrode compared to single BSCF catalyst.[160] Carbons suffer from strong corrosion at the typical OER potentials resulting in a high anodic corrosion current not only due to OER.[160, 161] Therefore, as already mentioned they must be avoided as conductive agent for a correct evaluation of the oxygen evolution activity.

So far, only few fundamental studies using perovskite thin films with controlled surface termination have been reported. Raabe et al.[162] performed an in-situ electrochemical electron microscopy study on $Pr_{1-x}Ca_xMnO_3$ perovskites revealing an essential role of the oxygen vacancy formation in the OER. Furthermore, the highest oxygen evolution activity was found for $0.3 \leq x \leq 0.5$ when the perovskite shows p-type semiconducting behaviour.[162] An additional study on thin film model electrodes has been carried out by Kome et al.[163] on $La_{0.8}Sr_{0.2}CoO_3$. The authors show that the (110) oriented film has the highest activity and also the highest formation of oxygen defects (lattice expansion) compare to the (111) and (100) oriented films.

Theoretical calculations have also recently brought a deeper understanding of the relation between perovskite oxygen evolution activity and surface/band structure properties. The DFT calculations performed by Man et al.[18] and already discussed in the previous paragraph (2.2) have shown a volcano plot correlation between oxygen evolution activity and surface intermediate binding energy. Again by DFT calculations Vojvodic and Nørskov[16] demonstrated a correlation between total number of occupied state (e_g and t_{2g} states) and adsorption energy of oxygen (**Figure 17**).

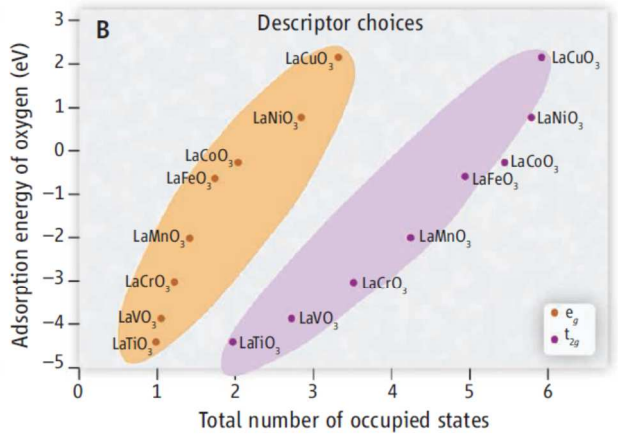

Figure 17 DFT calculations showing a correlation between the adsorption energy of oxygen species and the total number of occupied states. These results indicate that either the eg and the t2g symmetry occupation shows a correlation with the oxygen adsorption energy. Reproduced with permission of ref.[16].

The authors suggested that while some reaction steps (such as formation of OH* and O*) can occur at high rate when O atoms interact more strongly with the surface, other reaction steps become faster for low adsorption energy of oxygenated species. In agreement with the volcano plot of Man et al.[18], the best catalyst would be again the one showing the optimal compromise in the surface-oxygen interaction energies (Sabatier principle). Furthermore, by DFT calculation Vojvodic and Nørskov[16] indicated that the oxygen adsorption energies are not only correlated to the occupancy of the e_g but also of the t_{2g} energy levels. Particularly, only the reactive states near the Fermi level will interact with the adsorbate O 2p levels influencing the oxygen adsorption energy and hence the oxygen evolution activity. According to this statement, it has been recently shown[159] that among the family of double perovskites the composition $PrBaCo_2O_{5+d}$ with the O p-band centre very close to the Fermi level can display very high oxygen evolution activity

Conclusion & Outlook

As a consequence of the future fossil fuel depletion and the energy policies of several countries to abandon nuclear energy (such as Germany, Australia, Sweden, Belgium, Switzerland, and Italy) the upcoming electric power supply will rely to a larger extent than today on fluctuating primary solar and wind energy. Hydrogen as an energy vector will play a significant role due to its long term storage capability and flexibility since it can serve both for automotive and stationary applications, i.e. electromobility and power-to-gas conversion, respectively. Furthermore, H_2 can be directly converted into electrical energy by a fuel cell device but also used to produce syngas.

To face a hydrogen-based energy economy, electrolyser development will play an essential role since these devices can produce pressurizes, pure H_2 with relatively high efficiency. The electrolyser technology is indeed already available in the market, as demonstrated by, e.g., Proton OnSite with a PEWE stack operating at 1.6 A/cm^2, 50 ˚C, and 13 bar for about 60.000 h without any detectable decay rate.[164] The DOE target for water electrolysis efficiency points to operate at 2 A/cm^2 with a cell potential of 1.5 V vs. RHE within 2017.[165] Being the anode one of the largest sources of cell efficiency loss, significant R&D[165] has been directed towards the development of more active and more stable catalyst systems. Both for acidic and alkaline application, materials composition and microstructure must be optimized to enhance the rate of the OER, thus minimizing the efficiency loss (and in the case of PEWEs the amount of noble metal catalysts). For many catalyst materials proposed in the present review, the material composition and morphology not only influence the catalyst activity toward the OER but also its corrosion stability. In several cases the higher the activity the lower the stability under typical oxygen evolution conditions; however, the origin of this reverse relationship between stability and activity is not yet fully understood. Understanding the parameters governing both the OER and the catalysts corrosion process, either via theoretical and experimental tools, can lead to the design of novel catalysts or simply to reach the best trade-off between activity and stability. It must be also emphasized that composition, material preparation/processing, and morphology are all factors responsible for the electrochemical activity, current selectivity and stability of oxygen evolution anodes and, thus, developments of advanced catalysts can be reached only if all these factors are fully identified and controlled.

Acknowledgement

The authors gratefully acknowledge the Swiss National Science Foundation within the Ambizione Program, the Competence Center Energy & Mobility Switzerland (CCEM-CH) through the project RENERG^2, as well as CTI and the Swiss Competence Center for Energy Research (SCCER) *Heat & Electricity Storage* for financial contributions to this work. The authors also gratefully acknowledge Umicore AG & Co KG for proving $IrTiO_2$ catalysts used for the measurements shown in **Figure 2** and Prof. Jan Rossmeisl, Technical University of Denmark, for fruitful discussions and for providing some figures included in the manuscript.

Notes and references

Electrochemistry Laboratory, Paul Scherrer Institut, 5232 Villigen PSI, Switzerland.

E-mail: emiliana.fabbri@psi.ch; thomasjustus.schmidt@psi.ch

1. H. Ibrahim, A. Ilinca and J. Perron, *Renewable and Sustainable Energy Reviews*, 2008, **12**, 1221-1250.
2. S. Trasatti, *Journal of Electroanalytical Chemistry*, 1999, **476**, 90-91.
3. R. de Levie, *Journal of Electroanalytical Chemistry*, 1999, **476**, 92-93.
4. K. E. Ayers, E. B. Anderson, C. Capuano, B. Carter, L. Dalton, G. Hanlon, J. Manco and M. Niedzwiecki, *ECS Transaction*, 2010, **33**, 3-15.

5. P. Millet, R. Ngameni, S. A. Grigoriev, N. Mbemba, F. Brisset, A. Ranjbari and C. Etiévant, *Int J Hydrogen Energ*, 2010, **35**, 5043-5052.
6. N. Ramaswamy and S. Mukerjee, *Advances in Physical Chemistry*, 2012, 17 pages.
7. R. Hagelüken, R. Drieselmann and K. Van den Broeck, *Availability of Metals and Materials, in Precious Materials Handbook, Umicore Ag & Co. KG, Hanau-Wolfgang, Germany*, 2012.
8. Y. Matsumoto and E. Sato, *Materials Chemistry and Physics*, 1986, **14**, 397-426.
9. L. Brossard, *International Journal of Hydrogen Energy*, 1992, **17**, 671-676.
10. M. E. G. Lyons and S. Floquet, *Physical Chemistry Chemical Physics*, 2011, **13**, 5314-5335.
11. B. Lu, C. Wang, S. Chen, Y. Jinling, G. Wang and D. Cao, *Journal of Solid State Electrochemistry*, 2013, **17**, 2277-2282.
12. U. a. Paulus, T. J. Schmidt, H. a. Gasteiger and R. J. Behm, *J Electroanal Chem*, 2001, **495**, 134-145.
13. A. J. Bard and L. R. Faulkner, *Electrochemical Methods - Fundamentals and Applications*, Second Edi edn., JOHN WILEY & SONS, INC., New York • Chichester • Weinheim • Brisbane • Singapore • Toronto, 2001.
14. C. C. L. McCrory, S. Jung, J. C. Peters and T. F. Jaramillo, *J Am Chem Soc*, 2013, **135**, 16977-16987.
15. J. O. M. Bockris and T. Otagawa, *Journal of Electrochemical Society*, 1984, **131**, 290-302.
16. A. Vojvodic and J. K. Norskov, *Science*, 2011, **334**, 1355-1356.
17. H. Dau, C. Limberg, T. Reier, M. Risch, S. Roggan and P. Strasser, *ChemCatChem*, 2010, **2**, 724-761.
18. I. C. Man, H.-Y. Su, F. Calle-Vallejo, H. A. Hansen, J. I. Martínez, N. G. Inoglu, J. Kitchin, T. F. Jaramillo, J. K. Nørskov and J. Rossmeisl, *ChemCatChem*, 2011, **3**, 1159-1165.
19. M. T. M. Koper, *Journal of Electroanalytical Chemistry*, 2011, **660**, 254-260.
20. M. T. M. Koper, *Journal of Solid State Electrochemistry*, 2013, **17**, 339-344.
21. J. Rossmeisl, A. Logadottir and J. K. Nørskov, *Chemical Physics*, 2005, **319**, 178-184.
22. J. Rossmeisl, K. Dimitrievski, P. Siegbahn and J. K. Nørskov, 2007, 18821-18823.
23. J. Rossmeisl, Z. W. Qu, H. Zhu, G. J. Kroes and J. K. Nørskov, *Journal of Electroanalytical Chemistry*, 2007, **607**, 83-89.
24. J. O. M. Bockris, *The Journal of Chemical Physics*, 1956, **24**, 817.
25. A. I. Krasil'shchkov, *Zh. Fiz. Khim.*, 1963, **37**, 273.
26. W. H. Wade and N. Hackerman, *T Faraday Soc*, 1957, **53**, 1636-1647.
27. W. E. O'Grady, C. Iwakura, J. Huang and E. Yeager, ed. M. W. Breiter, The Electrochemical Society, Princeton, Editon edn., 1974, p. 286.
28. W. E. O'Grady, C. Iwakura and E. Yeager, *American Society of Mechanical Engineers*, 1976, **76 -ENAs-37**.
29. S. Trasatti, *Electrochimica Acta*, 1984, **29**, 1503-1512.
30. P. Sabatier, *Berichte der deutschen chemischen Gesellschaft*, 1911, **44**, 1984-2001.
31. N. M. Markovic, T. J. Schmidt, V. R. Stamenkovic and P. N. Ross, *Fuel Cells*, 2001, **1**, 105-116.
32. I. Katsounaros, J. C. Meier and K. J. J. Mayrhofer, *Electrochimica Acta*, 2013, **110**, 790-795.
33. A. R. Zeradjanin, N. Menzel, S. W. and P. Strasser, *Phys. Chem. Chem. Phys.*, 2014, **DOI: 10.1039/c4cp00896k**.
34. W. J. Albery and M. L. Hitchman, *Ring-Disc Electrodes*, Clarendon Press edn., OxFord, 1971.
35. K. Zeng and D. Zhang, *Progress in Energy and Combustion Science*, 2010, **36**, 307-326.
36. A. R. Zeradjanin, A. A. Topalov, Q. Van Overmeere, S. Cherevko, X. X. Chen, E. Ventosa, W. Schuhmann and K. J. J. Mayrhofer, *Rsc Adv*, 2014, **4**, 9579-9587.
37. R. Kötz, H. J. Lewerenz and S. Stucki, *J Electrochem Soc*, 1983, **130**, 825-829.
38. R. Kotz, S. Stucki, D. Scherson and D. M. Kolb, *Journal of Electroanalytical Chemistry*, 1984, **172**, 211-219.
39. S. Stucki, G. G. Scherer, S. Schlagowski and E. Fischer, *J Appl Electrochem*, 1998, **28**, 1041-1049.
40. R. Kötz, H. Neff and S. Stucki, *J Electrochem Soc*, 1984, **131**, 72-77.
41. T. Hepel, F. H. Pollak and W. E. O'Grady, *J Electrochem Soc*, 1985, **132**, 2385-2390.
42. A. Damjanovic, A. Dey and J. M. Bockris, *J Electrochem Soc*, 1966, **113**, 739-746.
43. M. H. Miles, E. A. Klaus, B. P. Gunn, J. R. Locker, W. E. Serafin and S. Srinivasan, *Electrochimica Acta*, 1978, **23**, 521-526.
44. M. H. Miles and M. A. Thomason, *J Electrochem Soc*, 1976, **123**, 1459-1461.
45. D. B. Rogers, R. D. Shannon, A. W. Sleight and J. L. Gillson, *Inorganic Chemistry*, 1969, **8**, 841-849.
46. R. S. Yeo, J. Orehotsky, W. Visscher and S. Srinivasan, *J Electrochem Soc*, 1981, **128**, 1900-1904.
47. M. W. Shafer, R. A. Figat, R. Johnson and R. A. Pollack, *30th ISE meeting,Trondheim, Extended Abstracts* 1977, 313.
48. N. M. Markovic, T. J. Schmidt, V. Stamenkovic and P. N. Ross, *Fuel Cells*, 2001, **1**, 105-116.
49. D. Galizzioli, F. Tantardini and S. Trasatti, *J Appl Electrochem*, 1974, **4**, 57-67.
50. D. Galizzioli, F. Tantardini and S. Trasatti, *J Appl Electrochem*, 1975, **5**, 203-214.
51. I. Katsounaros, S. Cherevko, A. R. Zeradjanin and K. J. J. Mayrhofer, *Angewandte Chemie International Edition*, 2014, **53**, 102-121.
52. L. D. Burke, O. J. Murphy, J. F. O'Neill and S. Venkatesan, *J. Chem. Soc., Faraday Trans. 1*, 1977, **73**, 1659-1671.
53. C. Iwakura, K. Hirao and H. Tamura, *Electrochimica Acta*, 1977, **22**, 329-334.
54. R. Kötz, H. J. Lewerenz, P. Brüesch and S. Stucki, *Journal of electroanalytical chemistry and interfacial electrochemistry*, 1983, **150**, 209-216.
55. J. Llopis and M. Vazquez, *Electrochimica Acta*, 1966, **11**, 633-640.
56. A. Damjanovic, A. Dey and J. O. M. Bockris, *Electrochimica Acta*, 1966, **11**, 791-814.
57. G. Lodi, E. Sivieri, A. Battisti and S. Trasatti, *J Appl Electrochem*, 1978, **8**, 135-143.
58. M. Pourbaix, *Atlas of electrochemical equilibria in aqueous solutions*, Pergamon Press, Oxford; New York, 1966.
59. S. Hackwood, L. M. Schiavone, W. C. Dautremont-Smith and G. Beni, *J Electrochem Soc*, 1981, **128**, 2569-2573.
60. B. Johnson, F. Girgsdies, G. Weinberg, D. Rosenthal, A. Knop-Gericke, R. Schlogl, T. Reier and P. Strasser, *J Phys Chem C*, 2013, **117**, 25443-25450.
61. T. Reier, I. Weidinger, P. Hildebrandt, R. Kraehnert and P. Strasser, *Electrochemical Synthesis of Fuels 2*, 2013, **58**, 39-51.
62. B. E. Conway and J. Mozota, *Electrochimica Acta*, 1983, **28**, 9-16.
63. S. Gottesfeld and S. Srinivasan, *Journal of electroanalytical chemistry and interfacial electrochemistry*, 1978, **86**, 89-104.
64. J. Mozota and B. E. Conway, *Electrochimica Acta*, 1983, **28**, 1-8.
65. D. A. J. Rand and R. Woods, *Journal of electroanalytical chemistry and interfacial electrochemistry*, 1974, **55**, 375-381.
66. T. Reier, M. Oezaslan and P. Strasser, *Acs Catal*, 2012, **2**, 1765-1772.
67. E. J. Frazer and R. Woods, *Journal of electroanalytical chemistry and interfacial electrochemistry*, 1979, **102**, 127-130.
68. R. Kötz and S. Stucki, *Electrochimica Acta*, 1986, **31**, 1311-1316.
69. G. Beni, L. M. Schiavone, J. L. Shay, W. C. Dautremont-Smith and B. S. Schneider, 1979.
70. X. Wu and K. Scott, *Int J Hydrogen Energ*, 2011, **36**, 5806-5810.
71. J. Xu, Q. Li, M. K. Hansen, E. Christensen, A. L. Tomás García, G. Liu, X. Wang and N. J. Bjerrum, *Int J Hydrogen Energ*, 2012, **37**, 18629-18640.
72. J. Xu, D. Aili, Q. Li, E. Christensen, J. O. Jensen, W. Zhang, M. K. Hansen, G. Liu, X. Wang and N. J. Bjerrum, *Energ Environ Sci*, 2014, **7**, 820-830.
73. R. Kötz and S. Stucki, *J Electrochem Soc*, 1985, **132**, 103-107.
74. K. C. Neyerlin, G. Bugosh, R. Forgie, Z. C. Liu and P. Strasser, *J Electrochem Soc*, 2009, **156**, S6-S6.

75. R. Forgie, G. Bugosh, K. C. Neyerlin, Z. C. Liu and P. Strasser, *Electrochem Solid St*, 2010, **13**, D36-D39.
76. N. B. Halck, V. Petrykin, P. Krtil and J. Rossmeisl, *Physical Chemistry Chemical Physics*, 2014, **16**, 13682-13688.
77. C. P. De Pauli and S. Trasatti, *Journal of electroanalytical chemistry*, 2002, **538**, 145-151.
78. A. Marshall, B. Børresen, G. Hagen, S. Sunde, M. Tsypkin and R. Tunold, *Russian Journal of Electrochemistry*, 2006, **42**, 1134-1140.
79. H. N. Nong, L. Gan, E. Willinger, D. Teschner and P. Strasser, *Chemical Science*, 2014, **DOI: 10.1039/c4sc01065e**.
80. A. T. Marshall and R. G. Haverkamp, *Electrochimica Acta*, 2010, **55**, 1978-1984.
81. K. Kadakia, M. K. Datta, P. H. Jampani, S. K. Park and P. N. Kumta, *J Power Sources*, 2012.
82. O. I. Velikokhatnyi, K. Kadakia, M. K. Datta and P. N. Kumta, *The Journal of Physical Chemistry C*, 2013, **117**, 20542-20547.
83. K. Kadakia, M. K. Datta, O. I. Velikokhatnyi, P. Jampani, S. K. Park, S. J. Chung and P. N. Kumta, *J Power Sources*, 2014, **245**, 362-370.
84. R. Hutchings, K. Müller, R. Kötz and S. Stucki, *Journal of Materials Science*, 1984, **19**, 3987-3994.
85. A. T. Marshall, S. Sunde, M. Tsypkin and R. Tunold, *Int J Hydrogen Energ*, 2007, **32**, 2320-2324.
86. J. F. C. Boodts and S. Trasatti, *J Electrochem Soc*, 1990, **137**, 3784-3789.
87. L. A. Da Silva, V. A. Alves, S. Trasatti and J. F. C. Boodts, *Journal of electroanalytical chemistry*, 1997, **427**, 97-104.
88. J. R. Varcoe and R. C. T. Slade, *Electrochem Commun*, 2006, **8**, 839-843.
89. M. Shiels, *Fuel Cells Bulletin*, 2014, **2014**, 4.
90. R. Subbaraman, D. Tripkovic, K.-C. Chang, D. Strmcnik, A. P. Paulikas, P. Hirunsit, M. Chan, J. Greeley, V. Stamenkovic and N. M. Markovic, *Nat Mater*, 2012, **11**, 550-557.
91. M. E. G. Lyons and M. P. Brandon, *International Journal of Electrochemical Science*, 2008, **3**, 1425-1462.
92. M. E. G. Lyons and M. P. Brandon, *International Journal of Electrochemical Science*, 2008, **3**, 1386-1424.
93. C. Iwakura, A. Honji and H. Tamura, *Electrochimica Acta*, 1981, **25**, 1319-1326.
94. B. S. Yeo and A. T. Bell, *J Am Chem Soc*, 2011, **133**, 5587-5593.
95. J. Ponce, E. Rios, J.-L. Rehspringer, G. Poillerat, P. Chartier and J. L. Gautier, *Journal of Solid State Chemistry*, 1999, **145**, 23-32.
96. J. Ponce, J. L. Rehspringer, G. Poillerat and J. L. Gautier, *Electrochimica Acta*, 2001, **46**, 3373-3380.
97. M. Srivastava, M. Elias Uddin, J. Singh, N. H. Kim and J. H. Lee, *Journal of Alloys and Compounds*, 2014, **590**, 266-276.
98. R. N. Singh, N. K. Singh and J. P. Singh, *Electrochimica Acta*, 2002, **47**, 3873-3879.
99. B. Lal, N. K. Singh, S. Samuel and R. N. Singh, *Journal of New Materials for Electrochemical Systems*, 1999, **2**, 59-64.
100. F. N. Büchi, M. Inaba and T. J. Schmidt, *Polymer Electrolyte Fuel Cell Durability; Eds.; Springer Science and Business Media LLC: New York* 2009, 199-221.
101. D. A. Corrigan, *Journal of Electrochemical Society*, 1980, **134**, 377-384.
102. L. Trotochaud, J. K. Ranney, K. N. Williams and S. W. Boettcher, *J Am Chem Soc*, 2012, **134**, 17253-17261.
103. M. E. G. Lyons, R. L. Doyle, I. Godwin, M. O'Brien and L. Russell, *J Electrochem Soc*, 2012, **159**, H932-H944.
104. S. L. Medway, C. A. Lucas, A. Kowal, R. J. Nichols and D. Johnson, *Journal of Electroanalytical Chemistry*, 2006, **587**, 172-181.
105. I. J. Godwin and M. E. G. Lyons, *Electrochem Commun*, 2013, **32**, 39-42.
106. H. Bode, K. Dehmelt and J. Witte, *Z Anorg Allg Chem*, 1969, **366**, 1-&.
107. H. Bode, K. Dehmelt and J. Witte, *Berich Bunsen Gesell*, 1963, **67**, 839-839.
108. H. Bode, K. Dehmelt and J. Witte, *J Electrochem Soc*, 1963, **110**, C69-C69.
109. M. E. G. Lyons and M. P. Brandon, *Journal of Electroanalytical Chemistry*, 2010, **641**, 119-130.
110. A. Delahaye-Vidal and M. Figlarz, *J Appl Electrochem*, 1987, **17**, 589-599.
111. M. S. Kim and K. B. Kim, *J Electrochem Soc*, 1998, **145**, 507-511.
112. P. W. T. Lu and S. Srinivasan, *J Electrochem Soc*, 1978, **125**, 1416-1422.
113. D. Cibrev, M. Jankulovska, T. Lana-Villarreal and R. Gomez, *Int J Hydrogen Energ*, 2013, **38**, 2746-2753.
114. M. R. Gennero de Chialvo and A. C. Chialvo, *Electrochimica Acta*, 1988, **33**, 825-830.
115. M. Cappadonia, J. Divisek, T. Von der Heyden and U. Stimming, *Electrochimica Acta*, 1994, **39**, 1559-1564.
116. M. F. Kibria and M. S. Mridha, *Int J Hydrogen Energ*, 1996, **21**, 179-182.
117. R. D. L. Smith, M. S. Prévot, R. D. Fagan, S. Trudel and C. P. Berlinguette, *J Am Chem Soc*, 2013, **135**, 11580-11586.
118. E. L. Miller and R. E. Rocheleau, *Journal of Electrochemical Society*, 1997, **144**, 3072-3077.
119. E. L. Miller and R. E. Rocheleau, *Journal of Electrochemical Society*, 1997, **144**, 1995-2003.
120. X. Li, F. C. Walsh and D. Pletcher, *Physical chemistry chemical physics : PCCP*, 2011, **13**, 1162-1167.
121. M. D. Merrill and R. C. Dougherty, *J Phys Chem C*, 2008, **112**, 3655-3666.
122. J. Landon, E. Demeter, I. Nilay, C. Keturakis, I. E. Wachs, R. Vasic, A. I. Frenkel and J. R. Kitchin, *Acs Catal*, 2012, **2**, 1793-1801.
123. M. W. Louie and A. T. Bell, *J Am Chem Soc*, 2013, **135**, 12329-12337.
124. L. Xu, Y.-s. Ding, C.-h. Chen, L. Zhao, C. Rimkus, R. Joesten and S. L. Suib, *Chem Mater*, 2008, **20**, 308-316.
125. S. H. Ahn, I. Choi, H.-Y. Park, S. J. Hwang, S. J. Yoo, E. Cho, H.-J. Kim, D. Henkensmeier, S. W. Nam, S.-K. Kim and J. H. Jang, *Chemical communications (Cambridge, England)*, 2013, **49**, 9323-9325.
126. G. W. Simmons, E. Kellerman and H. Leidheiser, *J. Electrochem. Soc.*, 1976, **123**, 1276-1284.
127. G. W. Simmons, A. Vértes, M. L. Varsányi and H. Leidheiser, *J. Electrochem. Soc.*, 1979, **126**, 187-189.
128. H. Willems, A. G. C. Kobussen, J. H. W. De Wit and G. H. J. Broers, *Journal of Electroanalytical Chemistry*, 1984, **170**, 227-242.
129. H. Willems, A. G. C. Kobussen, I. C. Vinke, J. H. W. De Wit and G. H. J. Broers, *Journal of Electroanalytical Chemistry*, 1985, **194**, 287-303.
130. G. Wu, N. Li, D.-R. Zhou, K. Mitsuo and B.-Q. Xu, *Journal of Solid State Chemistry*, 2004, **177**, 3682-3692.
131. I. Nikdov, R. Darkaoui, E. Zhecheva, R. Stoyanova, N. Dimitrov and T. Vitanov, *Journal of Electroanalytical Chemistry*, 1997, **429**, 157-168.
132. J. A. Koza, Z. He, A. S. Miller and J. A. Switzer, *Chem Mater*, 2012, **24**, 3567-3573.
133. M. Bajdich, M. García-Mota, A. Vojvodic, J. K. Nørskov and A. T. Bell, *J Am Chem Soc*, 2013, **135**, 13521-13530.
134. K. Fatih and B. Marsan, *Canadian Journal of Chemistry-Revue Canadienne De Chimie*, 1997, **75**, 1597-1607.
135. X. Wu and K. Scott, *J Mater Chem*, 2011, **21**, 12344-12344.
136. J. Jia, X. Li and G. Chen, *Electrochimica Acta*, 2010, **55**, 8197-8206.
137. R. Berenguer, A. La Rosa-Toro, C. Quijada and E. Morallón, *J Phys Chem C*, 2008, **112**, 16945-16952.
138. T.-C. Wen and H.-M. Kang, *Electrochimica Acta*, 1998, **43**, 1729-1745.
139. F. Rosalbino, S. Delsante, G. Borzone and G. Scavino, *Int J Hydrogen Energ*, 2013, **38**, 10170-10177.
140. Y.-S. Lee, C.-C. Hu and T.-C. Wen, *Journal of Electrochemical Society*, 1996, **143**, 1218-1225.
141. E. Rios, P. Chartier and J. L. Gautier, *Solid State Sciences*, 1999, **1**, 267-277.
142. S. Joiret, M. Keddam, X. R. Nóvoa, M. C. Pérez, C. Rangel and H. Takenouti, *Cement and Concrete Composites*, 2002, **24**, 7-15.
143. B. Messaoudi, S. Joiret, M. Keddam, H. Takenouti, M. Curie and C. P. Jussieu, *Electrochimica Acta*, 2001, **46**, 2487-2498.

144. Y. Miyahara, K. Miyazaki, T. Fukutsuka and T. Abe, *J Electrochem Soc*, 2014, **161**, F694-F697.
145. M. Morita, C. Iwakura and H. Tamura, *Electrochimica Acta*, 1979, **24**, 357-362.
146. K. Mette, A. Bergmann, J. P. Tessonnier, M. Havecker, L. D. Yao, T. Ressler, R. Schlogl, P. Strasser and M. Behrens, *Chemcatchem*, 2012, **4**, 851-862.
147. A. Bergmann, I. Zaharieva, H. Dau and P. Strasser, *Energ Environ Sci*, 2013, **6**, 2745-2755.
148. A. Ramírez, P. Bogdanoff, D. Friedrich and S. Fiechter, *Nano Energy*, 2012, **1**, 282-289.
149. M. M. Najafpour and D. J. Sedigh, *Dalton T*, 2013, **42**, 12173-12178.
150. T. Wolfram and S. Ellialtioglu, *Electronic and Optical Properties of d-Band Perovskites*, Cambridge University Press, 2006.
151. Y. Matsumoto, S. Yamada, T. Nishida and E. Sato, *Journal of Electrochemical Society*, 1980, **127**, 2360-2364.
152. T. Otagawa and J. O. M. Bockris, *J Electrochem Soc*, 1982, **129**, 2391-2392.
153. J. O. M. Bockris and T. Otagawa, *Journal of Physical Chemistry*, 1983, **87**, 2960-2971.
154. S. Trasatti, *Journal of Electroanalytical Chemistry*, 1980, **111**, 125-131.
155. J. Suntivich, K. J. May, H. A. Gasteiger, J. B. Goodenough and Y. Shao-Horn, *Science*, 2011, **334**, 1383-1385.
156. W. G. Hardin, S. D. A., X. Wang, S. Dai, K. P. Johnston and K. J. Stevenson, *The Journal of Physical Chemistry Letters*, 2013, **4**, 1254-1259.
157. C. Jin, X. Cao, F. Lu, Z. Yang and R. Yang, *Int J Hydrogen Energ*, 2013, **38**, 10389-10393.
158. C. Jin, X. Cao, L. Zhang, C. Zhang and R. Yang, *J Power Sources*, 2013, **241**, 225-230.
159. A. Grimaud, K. J. May, C. E. Carlton, Y.-L. Lee, M. Risch, W. T. Hong, J. Zhou and Y. Shao-Horn, *Nat. Comm.*, 2013, **4**, 2439-2439.
160. R. Mohamed, E. Fabbri, P. Levecque, R. Kötz, T. J. Schmidt and O. Conrad, *Ecs Transactions*, 2014, **58**, 9-18.
161. E. Fabbri, A. Rabis, R. Kotz and T. Schmidt, *Physical Chemistry Chemical Physics*, 2014, **16**, 13672--13681.
162. S. Raabe, D. Mierwaldt, J. Ciston, M. Uijttewaal, H. Stein, J. Hoffmann, Y. Zhu, P. Blöchl and C. Jooss, *Adv Funct Mater*, 2012, **22**, 3378-3388.
163. M. Komo, A. Hagiwara, S. Taminato, M. Hirayama and R. Kanno, *Electrochemistry*, 2012, **80**, 834-838.
164. E. B. Anderson, K. E. Ayers, C. B. Capuano and S. Szymanski, *Long Life PEM Water Electrolysis Stack Experience and Future Directions*, http://www.h2fc-fair.com/hm13/images/ppt/09tu/1530.pdf, Accessed May, 2014.
165. K. E. Ayers, C. B. Capuano and E. B. Anderson, *Ecs Transactions*, 2012, **12**, 15-22.